



Universiteit Utrecht

MSc. Thesis by Danny Do Quang - 5999340

Supervised by:

Dr. Walter Immerzeel (UU) and Dr. Joseph Shea (UNBC)

The applicability of the Global Precipitation Mission to detect and assess extreme rainfall events

25-05-2018

Do Quang, D (Danny)



Source image: NASA

Abstract

The global precipitation measurement mission (GPM) is the latest precipitation remote sensing satellite by NASA and JAXA. This study aims to assess the applicability of the GPM during extreme events. In particular: Hurricane Harvey (25-29 August) and a monsoon event in North-East India (9-13 August). This study shows that GPM can quantify and understand different types of extreme events. Validation with local rain gauges showed that GPM had average to good correlation coefficients and good POD values. Furthermore, GPM shows that it can correctly capture the occurrence of extreme events. The precipitation peaks of Harvey can be captured accurately with, for example, a Nash-Sutcliffe Efficiency (NSE) value of 0.71 at Houston NWS. The precipitation peaks of the monsoon event are also captured accurately with a NSE value of 0.62 at Shah Amanat. However, some over- and underestimation occurs. However, this can be explained due to faulty gauge data and due to miss sampling because a satellite can only take a snapshot measurement of a continuously changing extreme event. The characteristics of Harvey and the monsoon event and their key differences can also be distinguished. The GPM displays Harvey as relatively short and singular event with relatively high precipitation intensity, whereas the monsoon event is displayed as a relatively larger event with lower precipitation intensity. Furthermore, GPM shows that it can detect orographically enhanced precipitation in the monsoon area. The GPM also established that during Harvey the precipitation amount is higher inland than overseas. However, this is mainly due to the position of the hurricane eyewall, which causes the differences in precipitation for the period of Harvey around the shore.

Table of Contents

Abstract	1
1. Introduction.....	4
1.1 Lacking precipitation measuring methods	4
1.2 Aim and research questions	6
2. Extreme rainfall events.....	7
2.1 Hurricanes	7
2.2 Monsoons	7
3. Satellite remote sensing of precipitation	9
3.1 Methods used to measure precipitation from outer space	9
3.2 Past satellite based precipitation projects	10
3.3 Satellite precipitation products	11
3.4 Global Precipitation Measurement (GPM).....	12
4. Method.....	14
4.1 Study areas	14
4.2 Station gauge data.....	15
4.3 GPM data.....	15
4.4 Validation	16
4.4.1 Pearson correlation over aggregated time periods	16
4.4.2 Categorical validation	17
4.4.3 Precipitation over time for representative stations.....	18
4.5 Data analysis – Characteristics	19
4.5.1 Magnitude & total precipitation	19
4.5.2 Precipitation rate.....	21
4.6 GPM measurements in mountainous terrains and at land-sea changes	22
4.6.1 Digital elevation map - MERIT	22
4.6.2 Extreme event and elevation changes	22
5. Results	24
5.1 Validation	24
5.1.1 Correlation: GPM vs Gauges.....	24
5.1.2 Categorical validation	26
5.1.3 Time series graphs.....	27
5.2 Comparison hurricane and monsoon	31

5.2.1 Magnitude & total precipitation	31
5.2.1 Precipitation rate.....	36
5.2.3 Summary: comparison hurricane and monsoon.....	39
5.3 GPM accuracy with changing surroundings during extreme event	39
5.3.1 Monsoon interaction with elevation.....	39
5.3.2 Harvey interaction with land.....	45
6. Discussion.....	50
6.1 Validation	50
6.2 Characteristics: Monsoon vs Harvey	52
6.3 GPM accuracy with changing surroundings	53
6.4 Limitations	53
7. Conclusion	55
8. Glossary	56
9. Acknowledgements	57
10. References.....	58

1. Introduction

Extreme rainfall events over the world have shown that precipitation can cause major economic damage and loss of life due to flooding. Recent examples of these extreme events are hurricane Harvey and the rainfall events in India, Bangladesh and Nepal during the summer monsoon. On 25 August 2017, hurricane Harvey was the first category 4 hurricane to make landfall in the United States since 2005 (NWS, 2017). Heavy precipitation, with recorded station totals up to 1650 millimeter (mm) occurred over four days causing major flooding and 68 direct fatalities in and around Houston (Blake and Zelinsky, 2018). The total economic damage is estimated to be \$125 billion making it the second costliest natural disaster in the United States, after hurricane Katrina (Blake and Zelinsky, 2018). The South-Asian summer monsoon (SASM) occurs every year between June and September. During the SASM in 2017 there were also several flooding events. One rainfall event stands out. From the 9th until the 13th of August, heavy precipitation caused major flooding and landslides in North-East India, Nepal and Bangladesh (Figure 1.1). It has been estimated that around 24 million people were affected and that more than 800 people have been killed (UN, 2017). The economic damage of the flooding is unknown but is expected to be very large.

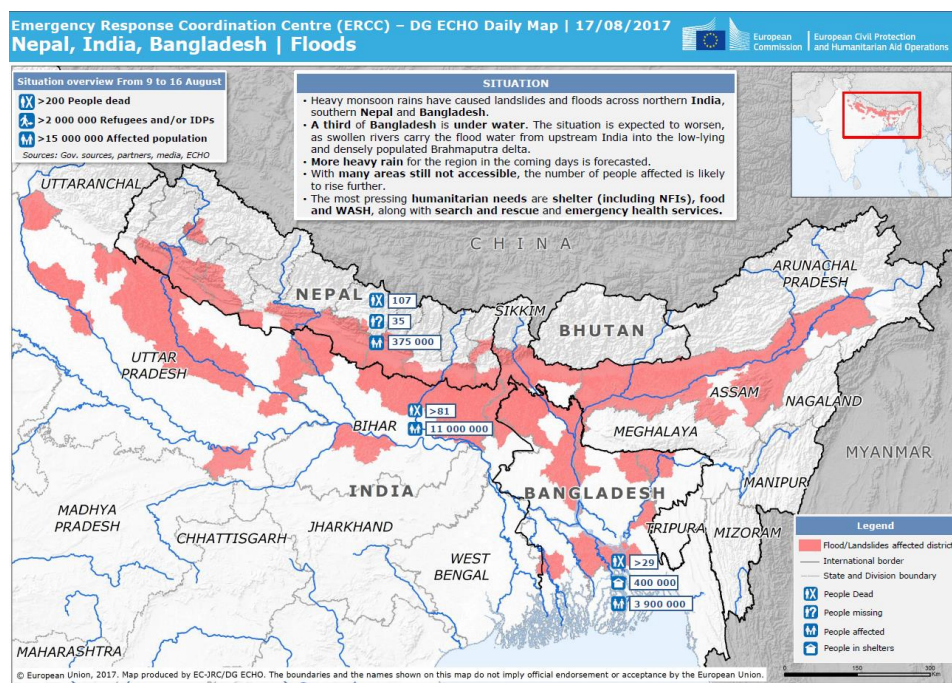


Figure 1.1: flood map of the Himalayan area during the storm that occurred in early August. (Source: ERCC, 2017)

1.1 Lacking precipitation measuring methods

The growing concern about climate change has increased the need for accurate tools to monitor impact of extreme events (New *et al.*, 2001). The tools that are presently used are often insufficient. There are several methods to measure precipitation at the moment: rain gauges, ground-based weather radars and satellites (Vasiloff *et al.*, 2007).

Rain gauges

The main advantage of rain gauges is their temporal coverage. Rain gauges provide a long and detailed record about trends and variability of precipitation throughout the 20th century. They are the most common approach for direct measurement of precipitation (New *et al.*, 2001). Rain gauges have poor

spatial coverage and often lacks data for most of the ocean regions, meaning that their coverage only amounts to about 25-30% of the world's surface (New *et al.*, 2001). Furthermore the gauges are prone to errors, the global under-catch was estimated to be 11%; these errors are mainly caused by wind and snow (Kidd and Huffman, 2011). Moreover, rain gauges in mountainous regions tend to be in the valleys, the rain gauge network may underestimate the orographically enhanced rainfall that occurs in mountain areas (Ebert, Janowiak and Kidd, 2007). Finding and fixing these errors is often a time consuming task, which is impossible to do at a global scale (New *et al.*, 2001).

Ground based radars

Ground-based radars have high spatial and temporal resolution and good areal coverage. There are weather radar data available on the order of 5km spatial resolution over 100,000 km² areas for every 10 minutes (Ferraro *et al.*, 1995; Harrison, Driscoll and Kitchen, 2000). Radars emit a low frequency beam of microwave energy, which is backscattered from particles in the atmosphere. The intensity of the returned signal is converted to a precipitation rate (New *et al.*, 2001). The use of weather radars has declined lately due to errors and uncertainty in the precipitation estimates (Harrison, Driscoll and Kitchen, 2000). These errors come from several factors. For example, the accuracy of a weather radar decreases as the distance increases (Vasiloff *et al.*, 2007). Radars also have bad coverage in complex terrain. Furthermore, ground based radars can measure contamination (e.g. aerosols) in the air as rain droplets, resulting in measurement errors (Vasiloff *et al.*, 2007).

Satellite remote sensing

Satellite remote sensing can measure precipitation in near real time with a continuous spatial coverage. They can provide estimates of precipitation in ungauged regions, such as oceans or remote areas. This is especially important for extreme events such as hurricanes, as they start from above the oceans. There are several techniques satellites can use to measure precipitation: visually, infrared, passive microwave, active microwave and multi sensor methods (Kidd and Huffman, 2011). With the latter three as the instruments of choice (Hou *et al.*, 2014). A major disadvantage of satellite remote sensing is that it has a significantly greater uncertainty than radar and gauge measurements. Which is why validation of satellite precipitation has been a major focus in recent years (eg. Nicholson *et al.*, 2003; Ebert, Janowiak and Kidd, 2007; Liao and Meneghini, 2009; Liu *et al.*, 2015).

The Global Precipitation Measurement

The Global Precipitation Measurement (GPM) is the latest precipitation satellite launched by NASA and JAXA in 2014. The GPM is designed to be the next-generation satellite precipitation observation method (NASA, 2017). The GPM can measure precipitation with a spatial resolution of 0.1°. The Integrated Multi-satellitE Retrievals for GPM (IMERG) is the algorithm which compiles the precipitation images into a dataset which has a half-hourly output in millimeter per hour [mm/h]. When the GPM is combined with other satellites, the precipitation of the entire globe can be measured every two to three hours (NASA, 2017). This latest iteration of satellite remote sensing can provide new and improved information about precipitation during extreme events. How IMERG is compiled and how GPM measures precipitation will be further elaborated in section 3.4.

1.2 Aim and research questions

The aim of this study is to assess the usability of GPM data for extreme events, with a focus on Hurricane Harvey on the 25-29 August 2017 and the South Asian monsoon event on 9-13 August 2017. A considerable amount of work has already been done with the other past satellite measurement methods (Bookhagen and Burbank, 2006; Liu *et al.*, 2015; Katsanos, Retalis and Michaelides, 2016). The research with the GPM is not as extensive compared with other satellite based precipitation projects, since the GPM is relatively new. Studies have shown that GPM has promising results in measuring precipitation during heavy rainfall events (Liu, 2016; Prakash *et al.*, 2016, 2018; Sharifi, Steinacker and Saghafian, 2016) . However, studies conducted in North East India has stated that GPM has some difficulties in detecting precipitation due to orographic effects (Prakash *et al.*, 2018). Furthermore, the area lacks a dense gauge network making remote sensing an essential for precipitation measurement (Bookhagen and Burbank, 2010). Therefore, additional research on the GPM could prove to be useful since more knowledge about GPM, can lead to an overall increase in the quality of precipitation measurements and the prediction of extreme events.

This results in the following research question:

Can data from the Global Precipitation Mission be used to quantify the distribution and magnitude of different types of extreme events?

The following sub questions will also be asked to help answer the main research question:

- How well does the GPM represent extreme events such as a monsoon and a hurricane?
- What are the key differences in GPM precipitation characteristics (magnitude, total precipitation and intensity) between a hurricane and a monsoon extreme event?
- How accurate are satellite derived estimates in mountainous terrains and at land-sea changes?

2. Extreme rainfall events

2.1 Hurricanes

Tropical cyclones are rapidly rotating storms that form over the ocean that have a characteristic low-pressure center, which is often referred to as the eye of the storm (Graham and Riebeek, 2006a). They are classified as a typhoon, cyclone or hurricane depending on the location where the storm originates. A hurricane is a counterclockwise storm that forms over the Atlantic Ocean during the summer and early fall. Its intensity will determine if it can be classified as a hurricane. A hurricane is defined as a tropical cyclone where the maximum sustained surface wind is 117 km/h (National Weather Service, 2014). The hurricane is formed over warm water, typically 26.5°C or higher (Graham and Riebeek, 2006a).

A hurricane or tropical cyclone is formed due to a positive feedback mechanism: When warm and moist air rises it causes condensation of rain droplets and thus releasing latent heat. This heat increases the buoyancy of the air parcel even more causing a greater rise (Graham and Riebeek, 2006b). A low-pressure area is then formed at the surface due to the rising air. Air from the surrounding areas will descend into that low-pressure area. The pressure at the top of the warm rising air increases and will be pushed outwards. Since there is an outflow of air, the pressure at the surface will decrease even more, therefore more air will be converged at the center of the storm, creating the eye of the storm (Figure 2.1). The intensity of the storm increases as the air spreads out more; it will increase the pressure drop at the center, triggering stronger winds higher (Graham and Riebeek, 2006b). The wind intensity increases towards the center of the low-pressure center of the storm, drawing more heat and moisture from the warm ocean surface. The distinctive spiral movement of the storm is due to the Coriolis force due to the rotation of the Earth. As the air moves to the center of the storm it will curve right creating a counterclockwise movement (Graham and Riebeek, 2006b).

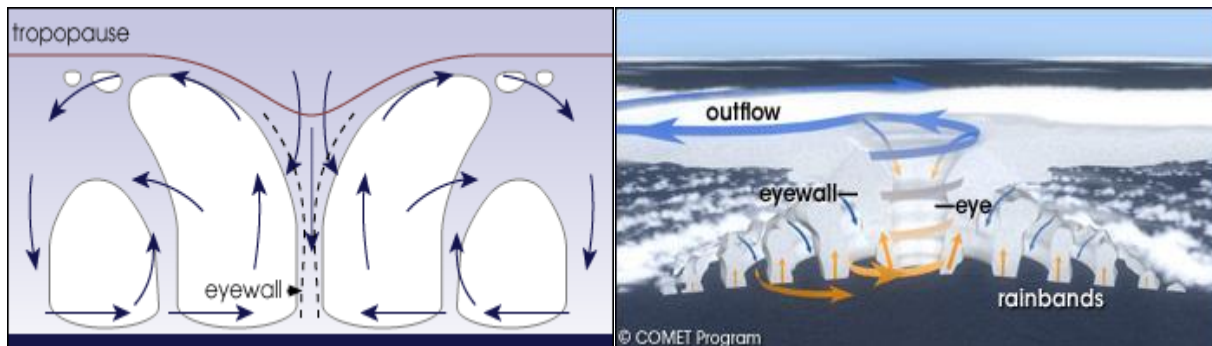
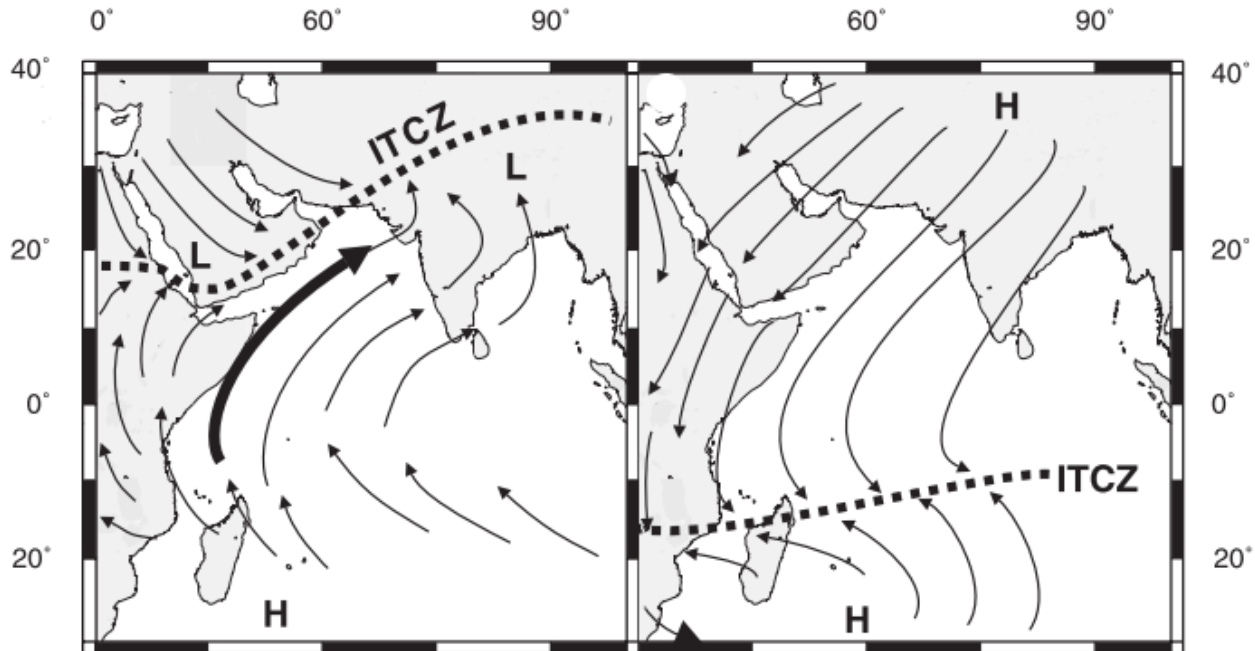


Figure 2.1: cross-section of a tropical cyclone (Graham and Riebeek, 2006b).

2.2 Monsoons

A monsoon is a seasonal wind pattern with associated precipitation that occurs in tropical and subtropical regions (IPCC, 2001a). There are three dominant monsoon systems in the world: The African, American and the Asian-Australian monsoons (IPCC, 2001b). For over 300 years, people thought that monsoons were gigantic land-sea breezes: During the summer land warms faster than the surrounding oceans. This would cause a pressure difference followed by a wind direction towards land, where warm and moist air would rain out (Webster *et al.*, 1998). However, studies have shown that monsoons are very complex. The earth's rotation and solar radiation have important roles in the inter-annual monsoon cycle, they cause the migration of the intertropical convergence zone (ITCZ), and this migration causes

trade winds to change direction (Figure 2.2). During the summer, the easterly trade winds change to a westerly trade wind causing the wind direction to go from ocean to land (Gadgil, 2003). Large-scale ocean–atmospheric mechanisms such as El Niño Southern Oscillation (ENSO) and the Northern Atlantic Oscillation (NAO) have also been correlated with monsoons. These global and atmospheric modes have shown that they can help predict precipitation of a monsoon (Webster *et al.*, 1998; Yang *et al.*, 2004; Annamalai, Hamilton and Sperber, 2007; Immerzeel and Bierkens, 2010).



*Figure 2.2: Migration of the ITCZ causing the trade winds to move. Left: summer situation; Right: winter situation. Source: (Fleitmann *et al.*, 2007)*

3. Satellite remote sensing of precipitation

3.1 Methods used to measure precipitation from outer space

There are several methods that satellites use to make precipitation measurements: VIS and IR methods, passive microwave methods, active microwave methods and multi sensor methods. This paragraph will briefly explain how these methods measure precipitation.

Visual (VIS)

VIS and IR are the oldest satellite remote sensing methods; therefore the longest record of this type of data is available (New *et al.*, 2001). VIS images are mainly used to identify cloudy areas, as clouds appear brighter than the Earth's surface due to albedo. VIS methods can identify convective clouds as thicker clouds reflect more light than thin clouds, making them more visible. This links cloud brightness with precipitation. This method is not always reliable as the relationship between clouds brightness and precipitation has proven to be poor. However identifying cloudy areas is still very important as it provides information on areas where it is not raining (Griffith *et al.*, 1978; Kidd and Huffman, 2011).

Thermal InfraRed (IR)

IR imagery shows the radiance of the earth surface and atmosphere. Thermal IR can determine the temperature and therefore the height of a cloud. Also, there is a consensus that cold clouds rain more than warmer clouds, therefore a first estimate of precipitation can be made. A relationship between precipitation and cloud temperatures can then be done through a statistical relationship or dynamic calibration (Griffith *et al.*, 1978; Kidd and Huffman, 2011).

Passive microwave (PMW)

Passive microwave measures natural thermal emission from rain particles. This method gives a stronger indication of precipitation than the VIS and IR methods; they provide information about the rain-particles inside the clouds. Two principles are used to measure precipitation. First, the emission of rain droplets leads to more microwave emission and the secondly ice droplets in clouds decrease the received microwave emission due to scattering of radiation. However, it should be noted that the former method is used over the ocean and that the second method is used over land (New *et al.*, 2001; Vasiloff *et al.*, 2007; Kidd and Huffman, 2011).

Active microwave (AMW)

Active microwave is the latest method to measure precipitation and offers the most direct method for satellite precipitation measurement. And uses microwave emissions to detect precipitation. The main difference with PMW is that active sensors generate radiation and registers the reflection of the particles in the clouds. A major advantage of this method is that different kinds of frequency bands can detect different kinds of hydrometeors. For example higher frequencies bands can detect snow (Kidd and Huffman, 2011).

Multi sensor methods

Multi sensor techniques use a combination of the techniques above to get optimized precipitation estimation. For example: only applying PMW on areas that an IR image has specified as a cloud.

3.2 Past satellite based precipitation projects

There have been several satellite based precipitation projects in the past. The World Meteorological Organization (WMO) has a database where all these projects have been categorized (WMO, 2017a). These satellites can be categorized in two types: Geostationary satellites and Low Earth Orbiting satellites.

Geostationary satellites (GEO)

GEO satellites orbit at the same rate as the Earth spins, meaning that they remain stationary at a respective location. GEO satellites can scan a large area of the earth surface, but the image degrades as the scan area widens (Kidd and Huffman, 2011). A few of the important GEO satellites at the moment are the Meteosat Second Generation satellites (MSG) that covers Europe, Africa and parts of the Atlantic and Indian Ocean (Schmetz et al., 2002). The Geo-stationary Operational Environmental Satellite (GOES) that mainly covers the western hemisphere (Menzel and Purdom, 1994), the Feng-Yun-2 satellites covers most of the eastern hemisphere just as the Japanese Multifunctional Transport Satellite (Himawari-8) and the Indian metrological satellite (Kalpana) (Bessho et al., 2016; WMO, 2017b). Table I summarizes the locations and specifications of several GEO satellites. These satellites have a few common traits: they all provide VIS image with a nominal resolution of 1 x 1 km and an IR image with resolutions around 4 x 4 km. They have a temporal resolution of 30 minutes, of their respective areas, although some GEO satellites like the MSG do this every 15 minutes. (Kidd and Huffman, 2011).

Table I: Summary of several past GEO satellites.

Satellite	Position	Sensor type	Channels	Spatial resolution (km)	Temporal resolution	Source
MSG	0° and 63°E	VIS-IR	11	1-3	15 min	(Schmetz et al., 2002)
GOES	75°W and 135°W	VIS-IR	5	1-4	30 min	(Menzel and Purdom, 1994)
Feng-Yun-2	105°E	VIS-IR	3	1-5	30 min	(WMO, 2017b)
Himawari-8	145°E	VIS-IR	5	1-2	30 min	(Bessho et al., 2016)
Kalpana	74°E	VIS-IR	3	2-8	30 min	(WMO, 2017b)

Low Earth Orbiting satellites (LEO)

The measurements LEO satellites often used to complement the GEO images. Most LEO satellites orbit the earth twice, providing information of their respective rotation twice. For example, The TRMM, covered 50°N–50°S of the world. However, it should be noted that most LEO satellites work with other satellites, giving the constellation global coverage. For example, the Meteorological operational satellites (MetOp) is such a constellation (WMO, 2017b). Another famous constellation is the Afternoon train (a-train) which the Aqua and CloudSAT were part of (NASA, 2018). Most of the LEO satellites have multichannel VIS, IR and PMW instruments to measure precipitation. Only the TRMM, CloudSAT and GPM have AMW instruments. There have been several important LEO satellites in the past and their instruments and general specifications will be elaborated in Table II.

Table II: Summary of past LEO satellites for precipitation measurement. Source: (Kidd and Huffman, 2011)

Satellite	Instruments	Measuring methods	Channels	Microwave bands (GHz)	Spatial resolution (km)	Temporal resolution	Source
TRMM	TMI	PMW	9	10–85	5-25	Twice 2 days	(NASA, 2017)
	PR	AMW	1	13.6	5	Twice 3 days	
NOAA/MetOP	AVHRR	VIS-IR	5	-	1	Twice daily	(WMO, 2017b)
	AMSU	PMW	5	23.8–183	20-50	Twice daily	
	MHS	PMW	5	89–190	17-50	Twice daily	
Aqua	MODIS	VIS-IR	36	-	0.25-1	Twice daily	(Parkinson, 2003)
	AMSR-E	PMW		6-89	5-25	Twice daily	
DMSP	SSMIS	PMW	7	19–183	13-45	Twice daily	(WMO, 2017b)
	SSM/I	PMW	11	19–85	12.5-25	Twice daily	
CloudSat	CPR	AMW	1	94 G	1.4	Once 16 days	(Stephens <i>et al.</i> , 2002)

3.3 Satellite precipitation products

By merging different kind data sources, satellite precipitation products can be made with varying spatial and temporal characteristics (Table III). Databases of satellite precipitation products can be categorized into two broad categories: 1,) A high spatial resolution precipitation product at a sub-daily or daily scale. 2,) Long-term precipitation products which are used for climatological purposes, sacrificing spatial and temporal resolution (Kidd and Huffman, 2011).

Table III: Summary of selected satellites and merged global precipitation products.

Product name	Data source	Coverage			Resolution	Source
		Spatial	Temporal	Spatial		
GPI	Geostationary IR	40°N–40°S	1986 – present	2.5°	Pentad and monthly	(Arkin and Meisner, 1987)
CMORPH	AMSU, MHS, SSM/I, TMI, AMSR-E	60°N–60°S	2002 – present	0.25°	Every 3 hours	(Al <i>et al.</i> , 2004)
GPCP	GPI, SSM/I, SSISMS, GPI	40°N–40°S	1979 – present	2.5°	Daily and monthly	(Adler <i>et al.</i> , 2003)
GSMaP	TMI, AMSR, SSM/I, GPI	60°N–60°S	1998 – present	0.1°	Every 30 minutes	(Kubota <i>et al.</i> , 2006)
CMAP	GPI, SSM/I, GPCP	90°N–90°S	1979 – present	2.5°	Pentad and monthly	(Xie and Arkin, 1996)
PERSIANN	GPI, TMI, PR	60°N–60°S	2001 – present	1°	Daily	(Sorooshian <i>et al.</i> , 2000)
TMPA	TMI, PR, AMSR, SSM/I, AMSU	50°N–50°S	1998 – present	0.25°	Every 3 hours	(Sorooshian <i>et al.</i> , 2000)
CHIRPS	TMPA, CMAP, Gauge data,	50°N–50°S	1981–present	0.05°	Daily, pentadal, and monthly	(Funk <i>et al.</i> , 2015)

3.4 Global Precipitation Measurement (GPM)

GPM is an LEO satellite launched by NASA and JAXA (Figure 3.1). The GPM is the successor of the Tropical Rainfall Measuring Mission (TRMM), and is designed as the next-generation observation method for precipitation (NASA, 2017). The GPM provides precipitation and snow measurements by using two advanced measuring instruments: the GPM Microwave Imager and the Dual-frequency Precipitation Radar.

GPM Microwave Imager (GMI)

The GMI is an PMW instrument which can measure up to 13 different microwave wavelengths, ranging from 10 GHz to 183 GHz (Hou *et al.*, 2014). The main difference with the TRMM is that the GMI has four high frequency wave channels (166 GHz to 183 GHz), higher frequency wavelengths are optimal to measure ice hydrometeors and the 183 GHz channel has proven to be less impacted by surface backgrounds (Kidd and Huffman, 2011). Another improvement is that the GMI has a 1.2 m diameter antenna, which allows the GMI to have a significantly better resolution over the TRMM (Table IV).

Dual-frequency Precipitation Radar (DPR)

The DPR is an AMW instrument which measures rainfall intensity and provides 3-dimensional images of rainclouds. The DPR uses two different wavelengths to measure precipitation: The Ku precipitation radar (KuPR), which has a frequency of 13.597 and 13.603 GHz, a resolution of 250m and measurement span of 245km. The Ka precipitation radar (KaPR), has a frequency of 35.547 and 35.553 GHz , a resolution of 250 and 500m and a measurement span of 120 km (Hou *et al.*, 2014). The KuPR uses almost the same wavelength as the TRMM; this means that the KuPR is a good extension of the TRMM observations for precipitation (NASA, 2017). The KaPR has two methods for scanning precipitation: one is the same as the KuPR, for the purpose of dual-wavelength retrieval. The other one has a higher resolution and a smaller measurement span, which is needed to measuring solid precipitation and light rain (Liao and Meneghini, 2011) .

The precipitation data measured by the GMI and DPR is then used as a reference standard. This data is enhanced by using other eight international of partner measurement satellites (NASA, 2017). Combining the GPM with the other satellites enables GPM to measure all precipitation of the entire globe every two to three hours (NASA, 2017).

Integrated Multi-satellitE Retrievals for GPM (IMERG)

The IMERG high-resolution database ($0.1^\circ \times 0.1^\circ$) is the near real-time sub-daily product that the GPM constellation provides after inter-calibrating, merging, and interpolating all microwave, infrared and gauge data available (Huffman *et al.*, 2018). The inputs for IMERG dataset are snapshots made by individual LEO satellite overpasses. These snapshots start as brightness temperatures, but are transformed into precipitation rate estimates using the Goddard Profiling Algorithm. This algorithm uses latent heat released by condensation and determines the relationship between latent heating and precipitation through statistical correlations (Olson *et al.*, 2004). All data is gridded and inter-calibrated to the GPM Combined Radar-Radiometer product with a 0.1° degree scale (CORRA) The gridded data is also combined into half-hourly fields and then provided to the CMORPH Kalman Filter Lagrangian time interpolation scheme (Joyce and Xie, 2011) and PERSIANN-CCS re-calibration scheme (Hong *et al.*, 2007) to create half hourly precipitation rate estimates. There are three IMERG products that result from the before mentioned steps: an early multi-satellite product (4 hours after observation time), a late multi-

satellite product (12 hours after observation time) and a final satellite-gauge product (after the monthly gauge data analysis is received 2.5 month after observation time). The gauges that are used for calibration are obtained from global data collections such as Climatic Research Unit (CRU), Food and Agriculture Organization (FAO) and the Global Historical Climatology Network (GHCN) for approximately 190 countries (Huffman *et al.*, 2018). This thesis uses the final satellite-gauge product.

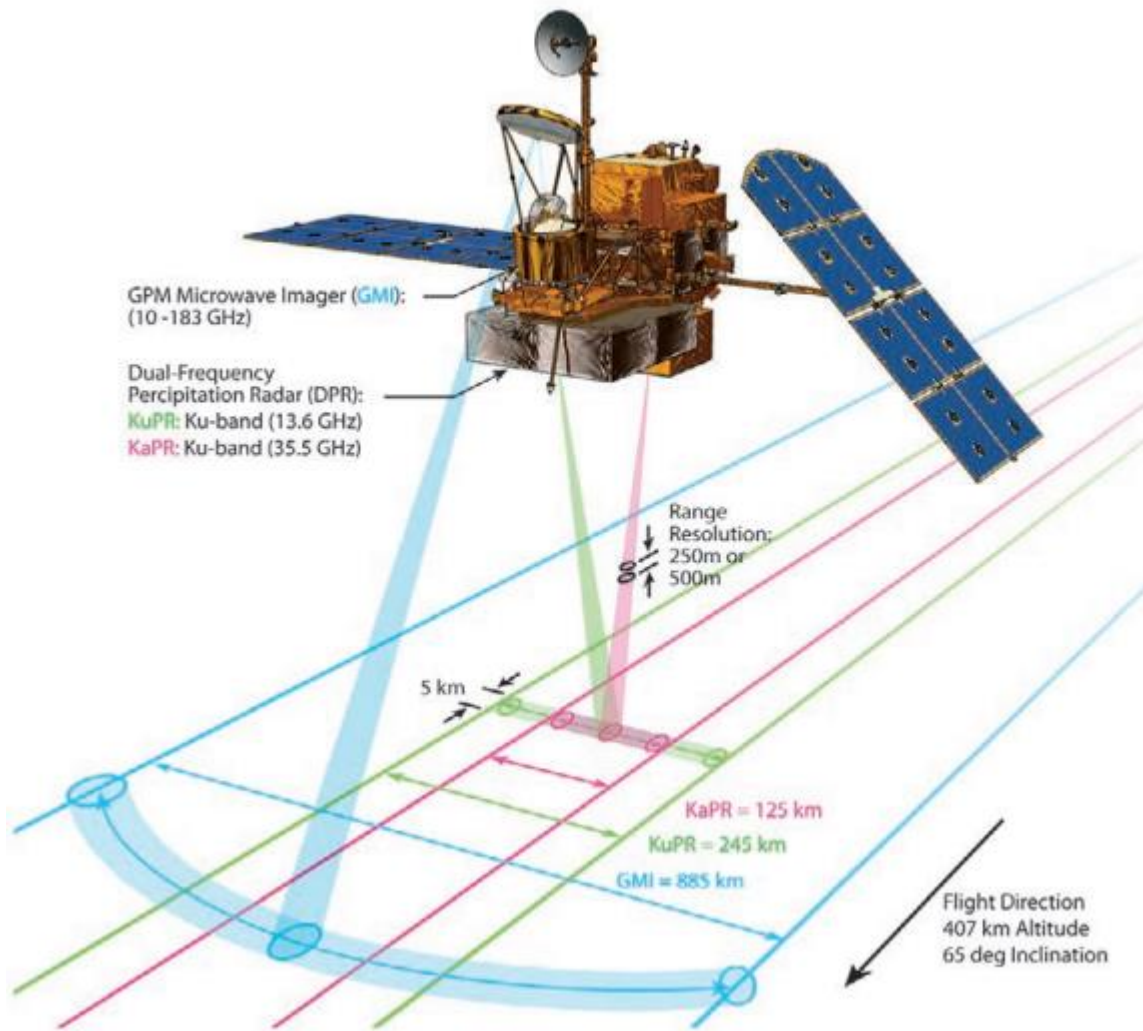


*Figure 3.1: A schematic of the scanning patterns and swaths of the DPR and GMI instruments on board the GPM Core Observatory (Hou *et al.*, 2014).*

4. Method

4.1 Study areas

Focus will be on two different study areas: Houston (Texas) and the Himalayas (North-East India, Nepal & Bangladesh) (Figure 4.1).

Hurricane area

The Houston area will be the study area for hurricane Harvey, since the hurricane made landfall near Houston. Furthermore, the amount of measurement stations in the Houston area is large, which means that the location is ideal for data analysis. The Houston region is located between longitudes 88°W and 100°W and latitudes 26°N and 33°N. The study area covers around 830 thousand square kilometers (Figure 4.1). The area is quite flat. The area has a slight elevation to the North-West: the elevation at Houston is around 27 meters and the highest point it is around 300 meter in the Northwest. The climate is classified as humid subtropical. The area is susceptible to tropical hurricanes every year during the hurricane season (June-November). Houston is the largest city in the area with the highest population of 2.3 million (United States Census Bureau, 2018).

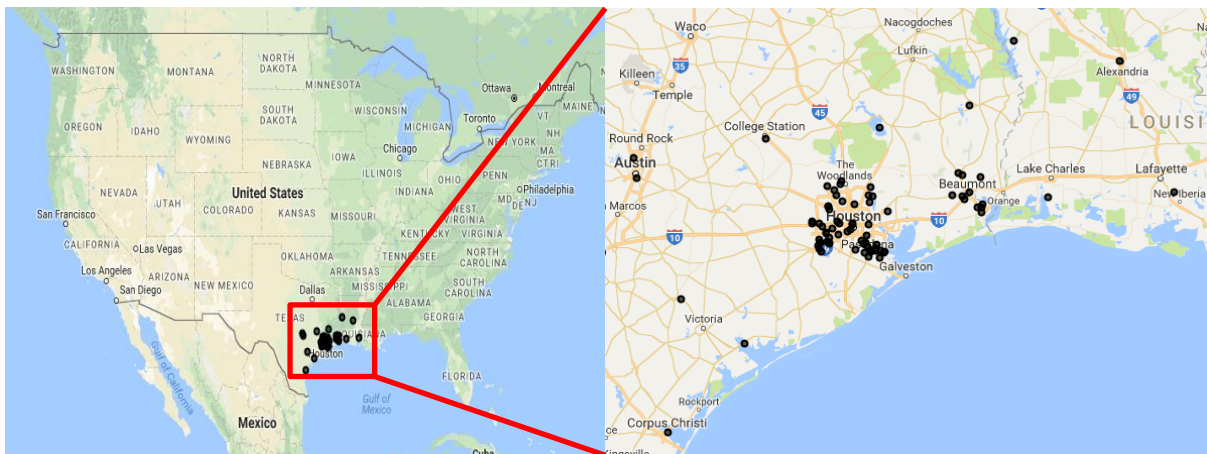


Figure 4.1: Houston area. Black dots show location of the GHCN and GSOD stations used for validation (Google Earth Engine, 2018).

Monsoon area

The Himalayas will represent the South Asian monsoon event that occurred on 9 - 13 August 2017. This will also be the study area where capability of the GPM in mountainous terrains will be tested. This study area is located between longitudes 75°E and 97°E and latitudes 20°N and 31°N. The study area covers 1.7 million square kilometers (Figure 4.2). The area is relatively low in NE-India and Bangladesh, where the elevation is around 20 to 200 meters. The elevation caused by the Himalayas start in Nepal. Where its topography will easily rise to a 1000 meter. The climate in this area is classified as humid subtropical. A summer monsoon occurs every year, due to a South-West trade wind which transports moist air into the area. There is a population of more than one billion million people in the study area (Bookhagen and Burbank, 2010).

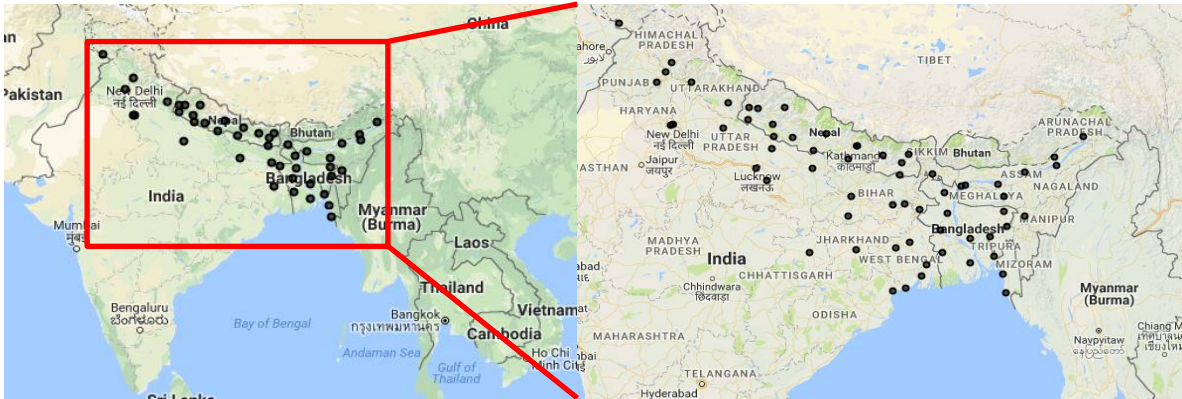


Figure 4.2: NE-India area. Black dots show location of the GHCN and GSOD stations used for validation (Google Earth Engine, 2018)

4.2 Station gauge data

The station precipitation data is obtained from the National Oceanic and Atmospheric Administration (NOAA) by using the Global Historical Climatology Network (GHCN) and the Global Surface Summary of the Day (GSOD) database. It should be noted that GPM uses the GHCN database to calibrate its precipitation output. The GHCN and GSOD provide the precipitation for each day per station for their respective research areas. There are 74 stations that can be used for the hurricane research area, 64 for the monsoon research area. The stations which are used in this research can be seen in the Appendix (Figure A1). All stations in the Houston research area are from the GHCN. This is also true for all stations in Bangladesh. The stations in Nepal are all acquired by the GSOD and the stations in India are from both databases. The data quality of these datasets depends on the location of the stations. The station data for the hurricane area is deemed to be good because the data in the Houston region is very comprehensive, whereas the station data in India is often incomplete making them unreliable. Furthermore, the concentration of the stations in the USA is quite dense, whereas the stations in India, Bangladesh and Nepal are more separated from each other. The precipitation data of the gauges is provided in millimeter per hour.

4.3 GPM data

The GPM data is obtained by using Google Earth Engine (GEE). The GPM dataset which is used is the Final version of IMERG v5. GEE is an open source platform which provides access to large geospatial datasets that can be processed on Google servers for specific regions and time periods (Gorelick *et al.*, 2016). The GPM dataset (IMERG) has a temporal resolution of 30 minutes and is measured in millimeter per hour. This means that there are two precipitation rates for one hour. Hence, the two precipitation rates per hour must be summed with each other and be divided by two to get an average hourly precipitation rate. The daily precipitation rate [mm/day] is obtained by summing the average hourly precipitation rates for that respective day. GEE also provides an Application programming interface (API) to analyze datasets. The API is used to obtain the precipitation measured by the GPM: each station has its own respective coordinates and these can be implemented in GEE. The GPM precipitation can then be extracted for each station location.

4.4 Validation

Three different validation methods are used: 1,) GPM against gauges. 2,) Categorical validation, based on the detection of precipitation. 3,) GPM and gauges against time at specific locations, which represent their respective extreme event.

4.4.1 Pearson correlation over aggregated time periods

GPM data are compared against gauge data with a simple correlation test. Both datasets are analyzed with R-Studio for this validation. These datasets are time aggregated into several time periods to see if the correlation changes depending on different time scales (extreme conditions vs normal circumstances). The timescales that are used are:

- Seasonal: June 1st until September 31
- Monthly: August
- 5 days around extreme event: 20 Aug - 3 Sep for Harvey and 4 – 18 Aug for Monsoon
- Extreme event: 25 - 29 Aug for Harvey and 9 - 13 Aug for Monsoon
- Daily: Every day during the extreme event (five times each day)

The precipitation of the GPM and the gauges are then plotted against each other with a 1:1 abline.

Pearson's correlation

Calculating the correlation coefficient needs two equally sized datasets. This however is not always possible, since gauge data is often missing or faulty. To compensate for this; the sum for each location is calculated for the GPM and gauge data respectively, while leaving the no data values out of the calculations. The cumulative precipitation is then divided with the amount of stations in each respective area to obtain an average precipitation rate. The averages for each location were used to calculate the correlation coefficient for each timescale. The correlation is calculated using the following formula Where x and y are the gauge and GPM data respectively and n the number of pairs:

$$r = \frac{n(\sum xy) - (\sum x)(\sum y)}{\sqrt{[n(\sum x^2) - (\sum x)^2][n(\sum y^2) - (\sum y)^2]}} \quad (1)$$

Percent Bias

The percent bias (PBIAS) was also calculated for every time scale. Bias is the average tendency of the simulated values to be smaller or larger than the observed value. In other words, a positive bias indicates overestimation and a negative bias indicates underestimation. In this case the simulated values are the GPM data points (y) and the observed values are the gauge data points (x). The PBIAS is calculated using the following formula:

$$PBIAS = 100 \frac{\sum_{i=1}^n (y_i - x_i)}{\sum_{i=1}^n x_i} \quad (2)$$

4.4.2 Categorical validation

The occurrence of precipitation is also evaluated by using a contingency table (Table IV). This method measures the precipitation that the GPM could detect by counting the hits (H), misses (M), false alarms (F) and correct negatives (N) to the precipitation of the gauges. This was done by changing all values of the GPM and the gauges with a positive value to 1 while leaving the zero values and then comparing them with each other with the contingency table. Four statistical indices are then calculated for all coupled GPM and gauge locations from June 1st until September 31. These four indices were also calculated for specific representative locations (Table V)

Table IV: contingency table to evaluate the occurrence of precipitation.

A/A		Satellite-GPM	
		Yes	No
Rain-gauge	Yes	<i>Hits (H)</i>	<i>Misses (M)</i>
	No	<i>False Alarm (F)</i>	<i>Correct Negative (N)</i>

Probability of detection

The probability of detection (POD) value represents the amount of precipitation that is correctly estimated by the GPM. The ideal score is 1 (Sharifi, Steinacker and Saghafian, 2016).

$$POD = \frac{H}{H + M} \quad (3)$$

False alarm ratio

The false alarm ratio (FAR) value represents the amount of precipitation that did not occur. The perfect score is 0 (Sharifi, Steinacker and Saghafian, 2016).

$$FAR = \frac{F}{H + F} \quad (4)$$

Critical success index

The critical success index (CSI) or treat score is also calculated. This value indicates how well the estimated/forecasted events correspond to the observed events (Sharifi, Steinacker and Saghafian, 2016).

$$CSI = \frac{H}{H + F + M} \quad (5)$$

The accuracy index

Last but not least, the accuracy index (ACC) is also estimated and this measures the fraction of correct estimates done by the GPM (Sharifi, Steinacker and Saghafian, 2016).

$$ACC = \frac{H + N}{H + F + M + N} \quad (6)$$

4.4.3 Precipitation over time for representative stations

The GPM is also validated over time by plotting the daily precipitation rate [mm/day] of the GPM and gauges over time that were measured at specific locations. Several stations were selected, for each extreme event, which are deemed as representative for Hurricane Harvey and the monsoon flood respectively (Figure 4.3 and Table V). The following criteria for these stations are set: There must be at least 80% of the gauge data available and the stations must be in an area where the precipitation is large. The GPM and gauge data are then both plotted against three different time scales to understand the timing of extreme event. The root mean squared error and Nash-Sutcliffe efficiency are also calculated for each these time scales:

- Seasonal (June 1st until September 31): To see how the GPM behaves when a lot of data points are taken into consideration, this can serve as a reference point as the “Normal” situation.
- Monthly (August): This is the month where both extreme event occur
- 5 days around extreme event (20 Aug – 3 Sep for Harvey and 4 – 18 Aug for Monsoon): the buildup to the extreme event and the aftermath of the extreme event.

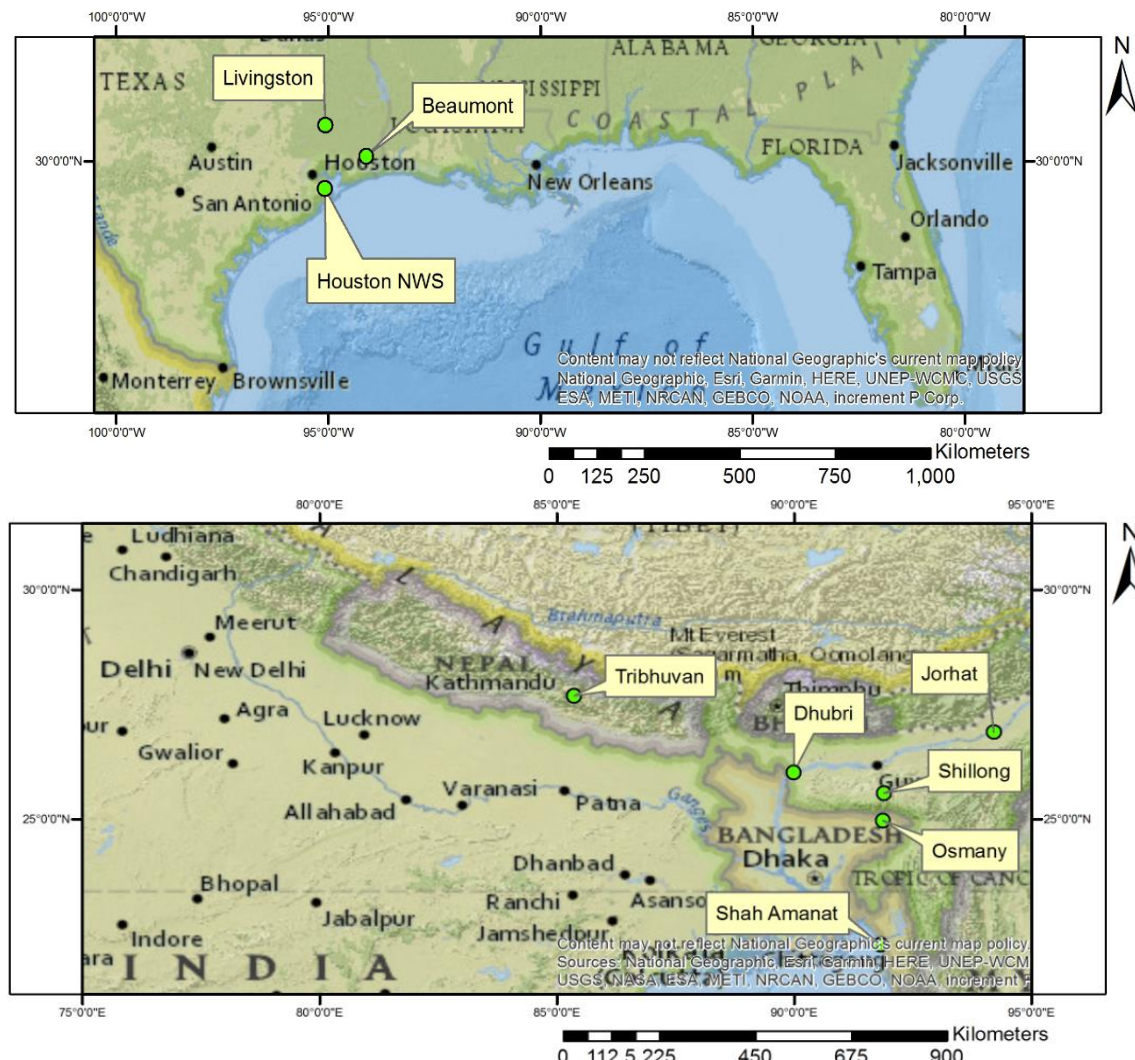


Figure 4.3 (Top): Representative Harvey stations in the USA. (Bottom): Representative Monsoon stations in India, Bangladesh and Nepal.

Table V: All representative stations used for data analysis

EE	Harvey	Monsoon		
Country	USA	India	Bangladesh	Nepal
Stations	Houston NWS, TX Beaumont, TX Livingston, TX	Jorhat Shillong Dhubri	Osmany Shah Amanat	Thibhuvan

Root mean squared error

The (root) mean squared error (RMSE) and the Nash-Sutcliffe efficiency (NSE) are commonly used criteria for evaluation and calibration of hydrological models and observed data (Gupta *et al.*, 2009). The RMSE represents standard deviation of the difference between simulated and observed values (Willmott, 1982). A small RMSE represents a better model performance. The RMSE is calculated using the following formula, where x and y are the gauge and GPM data respectively and n is the number of coupled GPM and gauge locations:

$$RMSE = [n^{-1} \sum_{i=1}^n (y - x)^2]^{0.5} \quad (7)$$

Nash-Sutcliffe efficiency

The Nash–Sutcliffe model efficiency (NSE) is used to assess the predictive power of hydrological models. The coefficient is a normalized statistic which represents the magnitude of the noise of the model against the measured data variance (Gupta *et al.*, 2009). The coefficients of the NSE range from minus infinity (INF) to 1, where 1 indicates a perfect match of the modelled to the observed data. If the NSE is zero, this indicates that the mean of the model is as accurate as the mean of the observed values. If the NSE value falls in between minus infinity and zero, it means that the mean of the observed values is better predictor than the model. The following formula is used where x and y are the gauge and GPM data respectively and n is the number of coupled GPM and gauge locations:

$$NSE = 1 - \frac{\sum_{i=1}^n (y_i - x_i)^2}{\sum_{i=1}^n (x_i - \bar{x})^2} \quad (8)$$

4.5 Data analysis – Characteristics

4.5.1 Magnitude & total precipitation

The differences in total precipitation [mm] measured by the GPM of each extreme event will be observed in this research. This is done by spatially analyzing total precipitation maps of both extreme event locations at a seasonal, monthly, extreme event and daily scale. The magnitudes of the extreme events were also analyzed using these maps. The maps that are used for the spatial analysis are extracted from GEE. An identical extraction extent is used for each extreme event: The extent is about 630,000 km² and encompasses the center of each respective storm. The longitude coordinates of the Harvey domain range from 90.7°W to 98.0°W and has latitude ranges between 25.1°N and 32.0°N. For the monsoon this area is between in the longitude ranges 85.7°E and 93.0°E and latitude ranges of 21.1°N and 28.0°N (Figure 4.4). This extent was chosen, because it encompasses the center of each event where most precipitation occurred.

The influence of the total precipitation that occurred during both extreme events within each domain will be analyzed by comparing them to the total precipitation that fell during the seasonal timescale. The total precipitation values are extracted from the stations that are all situated within each extreme event. Double mass plots are also constructed to evaluate the precipitation characteristics of the GPM and gauges and how they differ from each other when the extreme event occurs. These plots are constructed by plotting the total precipitation accumulation of the GPM against the total accumulation of the gauges. The total accumulation is calculated for the whole seasonal scale: 1 June until 31 September.

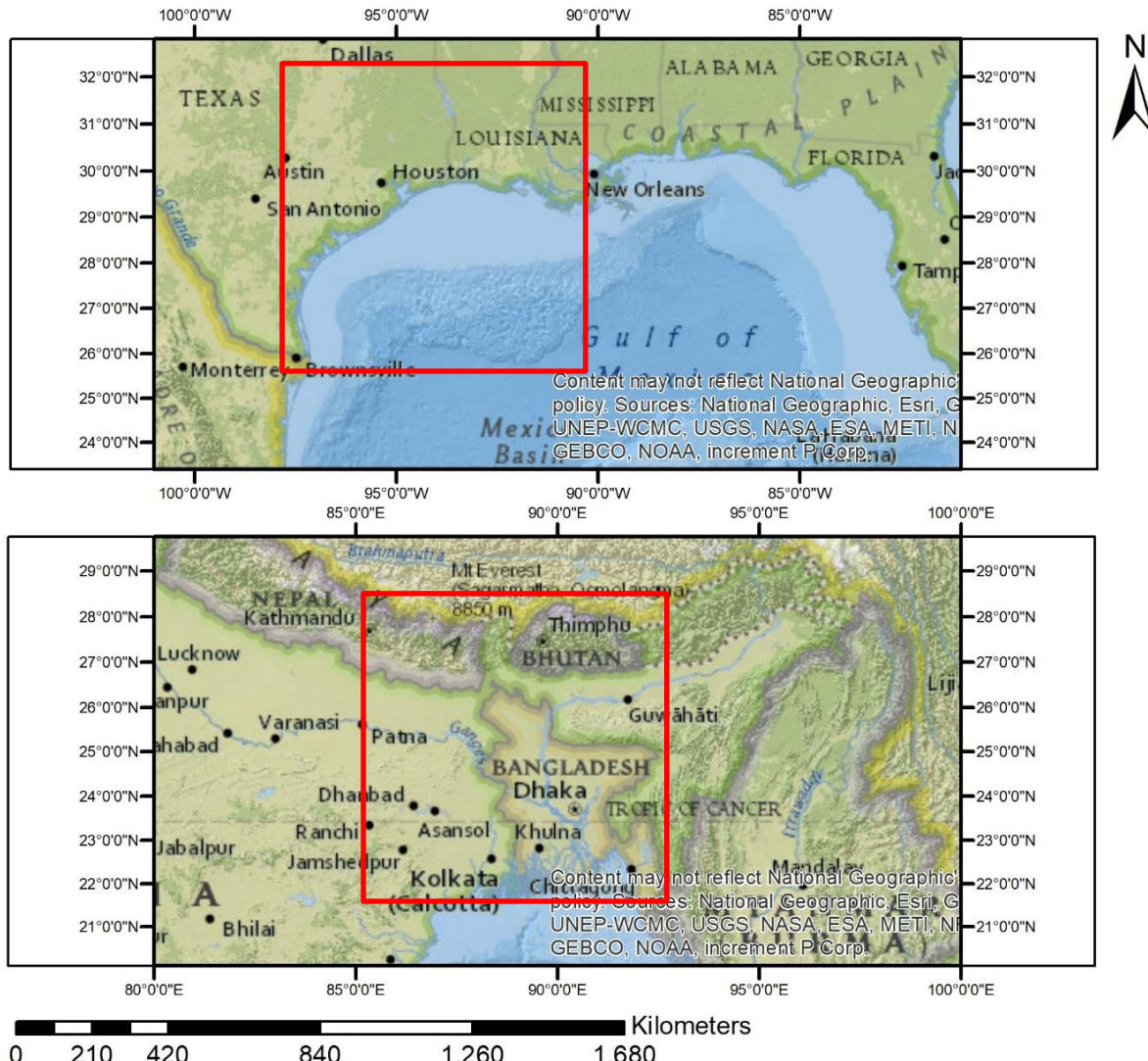


Figure 4.4: base maps with extraction domain for both extreme event locations.

4.5.2 Precipitation rate

Each domain was divided into 25 equal cells to be able to quantify and compare the precipitation rates [mm/h] within each respective domain. This was done because grids cells provide clear boundaries within the domain, which is essential for comparing the spread of the precipitation rate within the extreme events (Figure 4.5). Please note that doing this decreases the accuracy, however it does save computation time. The maximum and average precipitation rate [mm/h] of each cell was analyzed and compared for every timescale.

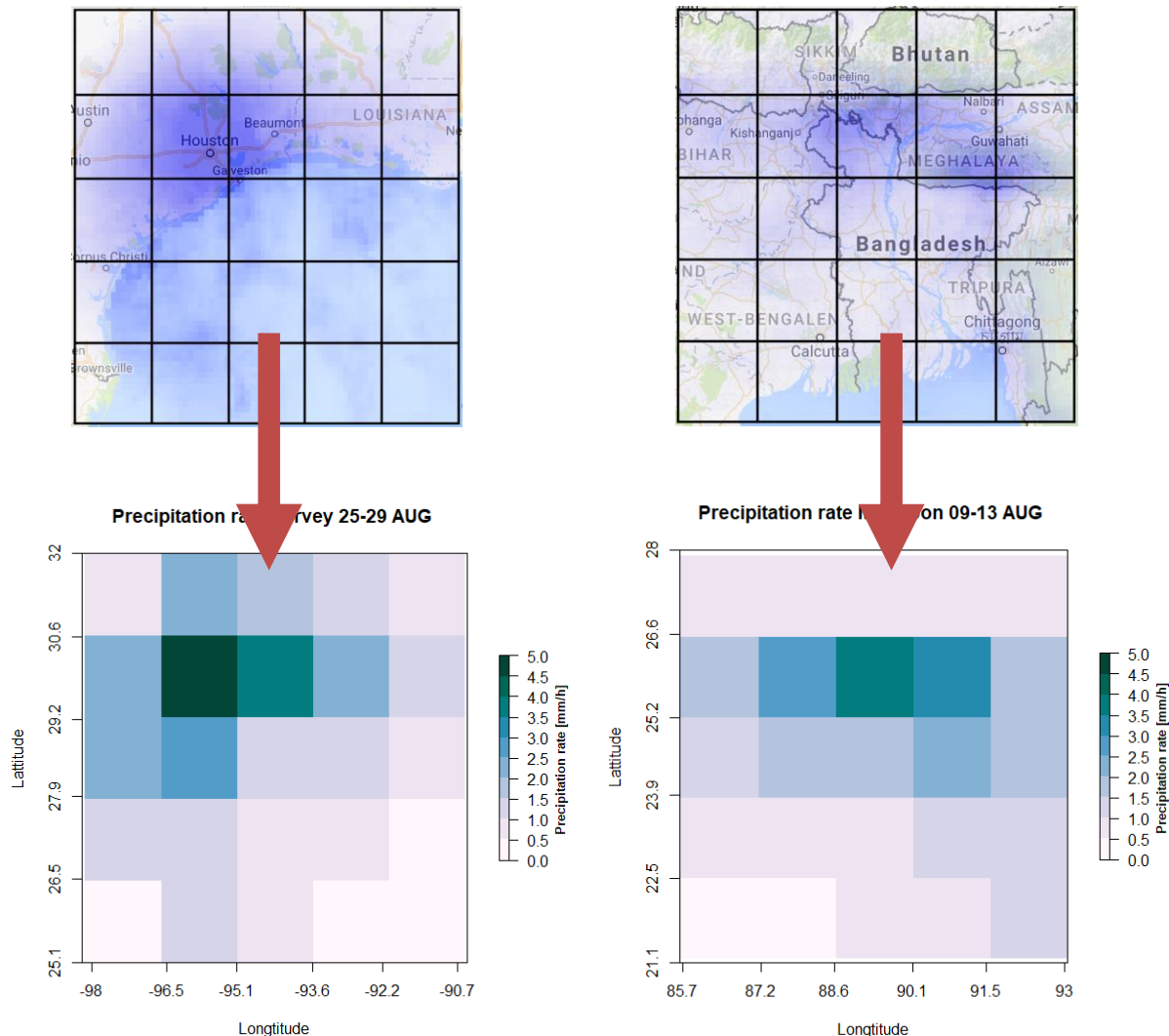


Figure 4.5: Houston domain (left) and the monsoon domain (right) with the upscaled gridded version.

Precipitation rate – frequency distribution

The precipitation intensity between the two extreme events will also be compared. This is done over the same domain used for the magnitude and total precipitation analysis (Figure 4.4). The aggregated precipitation rate [mm/h] for every half hour is extracted for the whole domain. Please note that the precipitation rates from the gridded cells are different compared to other precipitation rates used in this research, as some precipitation rates have been averaged over the whole domain. Histograms of these measurements will be made by plotting the frequency of sub-daily precipitation rates for different timescales. These are the monthly and extreme events timescales.

4.6 GPM measurements in mountainous terrains and at land-sea changes

4.6.1 Digital elevation map - MERIT

A digital elevation map (DEM) is needed to be able to assess GPM interaction with elevation. The DEM that is used for this research is the Multi-Error-Removed Improved-Terrain DEM (MERIT) which combines of several different DEMs to gain a more detailed DEM. The MERIT has a resolution of three arcseconds, which is about 90 meters at the equator. The Ice, Cloud, and land Elevation Satellite (ICESat) is used for reference ground elevation (Harding and Carabajal, 2005). The AW3D-30 m DEM (above 60°N) and the SRTM3 DEM (below 60°N) are used as a foundation for the MERIT (Farr *et al.*, 2007; Tadono *et al.*, 2016). The Viewfinder Panoramas DEM (VFP-DEM) is used to fill in the observational gaps (Gesch *et al.*, 2014). When all of these parts are combined it lowers the four major errors of DEMs: Speckle noise, stripe noise, absolute bias and tree height bias (Yamazaki *et al.*, 2017)

4.6.2 Extreme event and elevation changes

GPM maps for the monsoon event are exported from GEE to ArcMap. These maps are placed over the DEM. Three lines (green, red and blue) are drawn from south to north and perpendicular to the elevation. The respective lengths of these lines are approximately 575 km, 600 km and 595 km. Three Profiles are constructed of the DEM and the GPM precipitation during the extreme event (Figure 4.6). This is also done for the daily GPM measurements during the extreme events (Figure 4.6).

The GPM maps are evaluated across the land-ocean transition during Hurricane Harvey, the same process is done as at the monsoon domain: three lines (green, red and blue) are also drawn from south to north. The approximate lengths of these lines are 300 km, 650 km and 595 km respectively. The GPM precipitation of the hurricane and its daily totals are plotted along their respective DEM profiles where the land-sea transition will be analyzed (Figure 4.6 & 4.7). The ocean sea level is assumed to be zero, since the MERIT DEM doesn't have any sea level data.

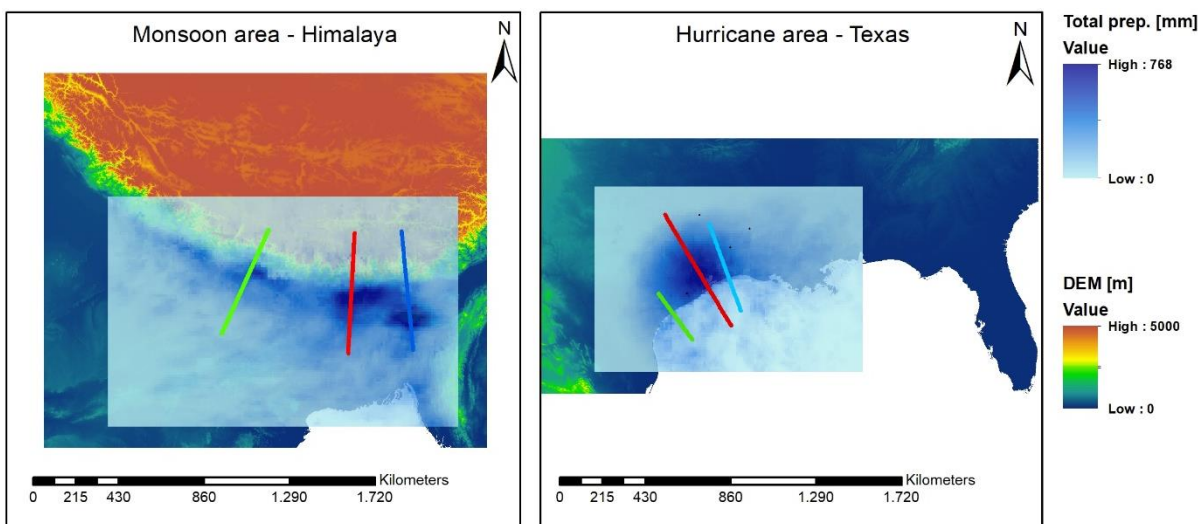


Figure 4.6: DEM maps of Monsoon and Harvey area with the overlaid GPM map (extreme event) and the three colored profiles.

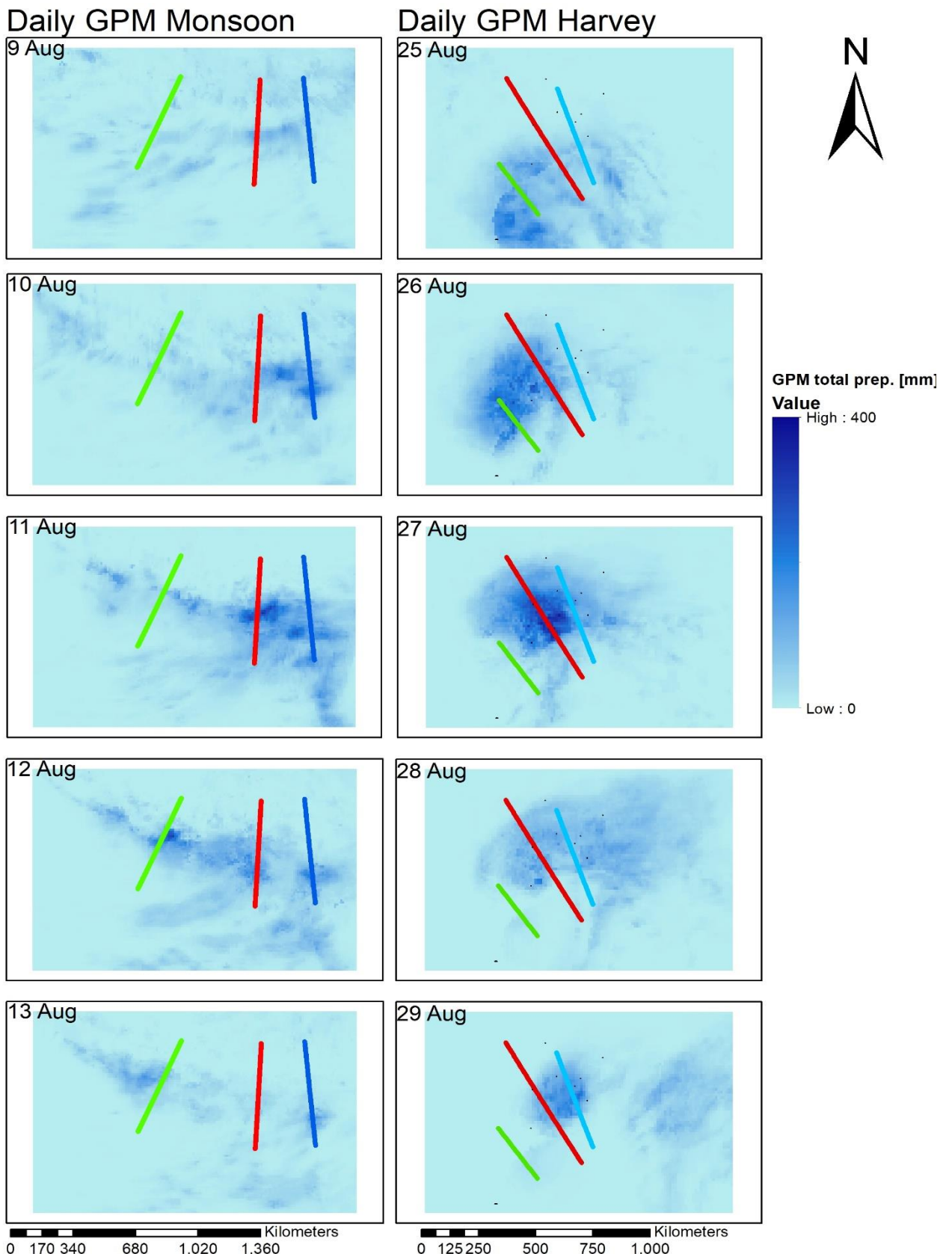


Figure 4.7: Daily GPM maps of Monsoon (left) and Harvey (right) area and the three colored profiles.

5. Results

This section will present the results of the research. The validation results will first be presented. The results of the difference in the precipitation characteristics between the two extreme events will be presented after that. Finally, the GPM interaction with elevation and land-ocean changes will be presented. It should be noted that figures not found in this section that can be found in the appendix. When these figures are discussed it will be indicated by an A.

5.1 Validation

5.1.1 Correlation: GPM vs Gauges

Harvey

The correlation coefficient (CC) increases as the timescales get smaller. This only amounts for the first four larger scales (seasonal, monthly, 5 days around extreme event and extreme event). The correlation graphs on the larger timescales indicate a major underestimation made by the GPM (Figure 5.1). This could be caused by faulty gauge data or due to miss-sampling precipitation during Harvey by the GPM. The underestimation is less visible in the daily timescale plots, where the spread is more consistent (Figure A2). However, GPM has a large overestimation on 25 August and an underestimation on 28 - 29 August. The correlation coefficient during these two days is lower respective to the other days (Table VI).

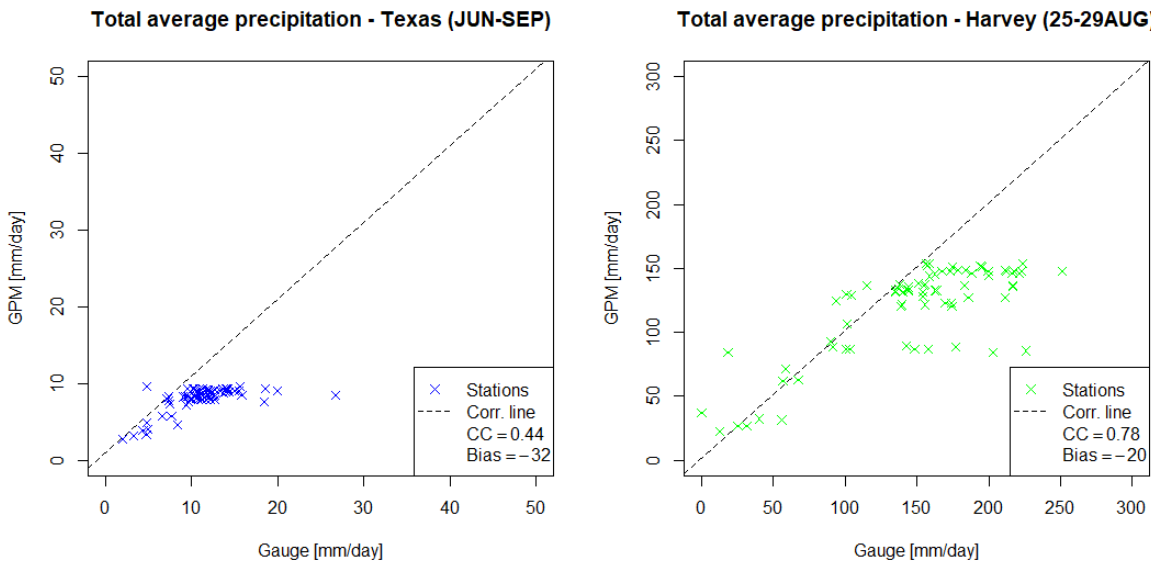


Figure 5.1: (left): Correlation plot of GPM vs gauges (June - September) - There is a clear cutoff around 10mm/day, which indicates an underestimation by the GPM. (right): Correlation plot of GPM vs gauges (25-29 August) – Cutoff is also visible at the y-axis around 150mm/day.

Monsoon

The correlation plots show that precipitation is better captured by the GPM in the monsoon region. There is no clear underestimation observable unlike the hurricane correlation plots. The monsoon values are more spread from the (1:1)-abline than in the hurricane plots (Figure 5.2). The correlation plots also show that the GPM often measures precipitation whereas the gauges indicate no precipitation (Figure 5.2). This overestimation by the GPM becomes more apparent as the timescales get smaller (Figure A3).

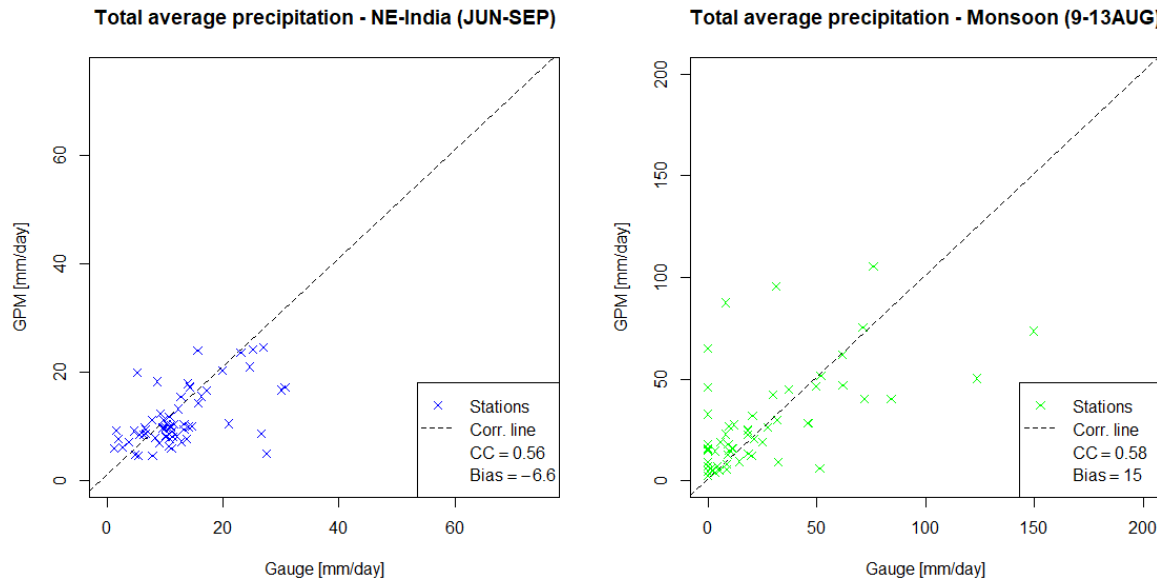


Figure 5.2: (left): Correlation plot of GPM vs gauges (June - September). (right): Correlation plot of GPM vs gauges (25-29 August).

Pearson's correlation

Overall it could be stated that the correlation between the GPM and the gauges is average. However, there are four instances where the correlation is close to one, meaning that GPM is able to correctly capture precipitation. The correlation of the monsoon area is better than of the hurricane area during the seasonal scale. However, this reverses as the timescales get smaller (Table VI). The correlation in both cases is highest during the extreme events. At the daily scales, the lowest correlation coefficients are calculated: 0.35 in the hurricane area and 0.32 in the monsoon area. But, there is also an instance with a high value for both cases (0.76 and 0.71 respectively).

Percent Bias

The percent bias was also calculated for both locations and timescales (Table VI). A negative bias indicates that the GPM underestimates the gauge values and vice versa. This underestimation dictates in the Harvey study area, since the bias has large negative values here. Observing the biases on a daily scale shows that GPM vastly overestimates precipitation during the first two days (very high positive values), however for the last three days of Harvey underestimation occurs again. The GPM overestimates the precipitation in the monsoon area for the larger scales except for the seasonal timescale. Just as in the hurricane area, a very large overestimation occurs during the first three days in the monsoon area, which then changes to an underestimation for the last few days of the monsoon. It should be noted that the bias in the monsoon area is relatively smaller than the bias in the hurricane area.

Table VI: All correlation indices (Total accumulation at all stations, Pearson's correlation coefficient and percent bias)

IMERG v5	Hurricane area			Monsoon Area		
	Period/Timescale	Total accumulation GPM [mm]	CC	PBIAS	Total accumulation GPM [mm]	CC
Seasonal	986	0.44	-32	1399	0.56	-7
August	697	0.5	-37	410	0.45	5.4
5 days around EE	628	0.58	-31	240	0.54	12
Extreme event	593	0.78	-20	142	0.58	15
Day 1	37	0.35	370	12	0.32	26
Day 2	135	0.5	58	34	0.42	140
Day 3	238	0.76	-6	42	0.45	10
Day 4	89	0.35	-56	35	0.71	-6
Day 5	95	0.47	-47	19	0.37	-25

5.1.2 Categorical validation

According to the POD statistics in Table VII, GPM captures about 79% of precipitation correctly in the hurricane area and about 93% in the monsoon area during June - September. The POD values calculated for the individual stations are also very high; however, the POD values of the monsoon gauges (approximately 99%) are all higher than those in the hurricane area (approximately 75%). The FAR values show, as expected, the exact opposite; the FAR is always higher in the hurricane areas than the monsoon area. The CSI values act like the POD values, the CSI are always lower at the hurricane areas than the monsoon area. The ACC values also show that GPM is better at capturing precipitation in the monsoon area (72%) than in the hurricane area (68%). This also translates back when assessing the individual stations per respective study area: the overall accuracy is better at the individual monsoons stations than at the individual stations hurricane stations.

Table VII: All statistical indices (POD, FAR, CSI and ACC)

	POD	FAR	CSI	ACC
Hurricane area	0.79	0.49	0.45	0.68
Monsoon area	0.93	0.26	0.70	0.73
Houston NWS	0.81	0.44	0.50	0.71
Beaumont	0.78	0.40	0.51	0.69
Livingston	0.94	0.61	0.38	0.61
Dhubri	0.97	0.21	0.77	0.77
Jorhat	0.99	0.17	0.82	0.82
Shillong	0.99	0.16	0.83	0.83
Osmany	1.00	0.10	0.90	0.91
Shah Amanat	0.98	0.26	0.73	0.73
Tribhuvan	1.00	0.32	0.68	0.72

5.1.3 Time series graphs

Harvey stations - USA

The timeseries of the GPM precipitation and the gauges show remarkable results. The plots show that the GPM is good at capturing Harvey. This is especially noticeable in the Houston NWS plots, where the peak of the extreme event (EE) is almost perfectly captured (Figure 5.3). However, it should be noted that the GPM does not perfectly capture the precipitation; there are some instances where the GPM underestimates the precipitation. The GPM correctly captures the temporal precipitation fluctuations of Harvey at Beaumont; however, it significantly underestimates the precipitation amount of the extreme (Figures A5). At the Livingston station another phenomenon occurs, the peak of the EE is almost perfectly captured, but it is captured a day too soon (Figure 5.3).

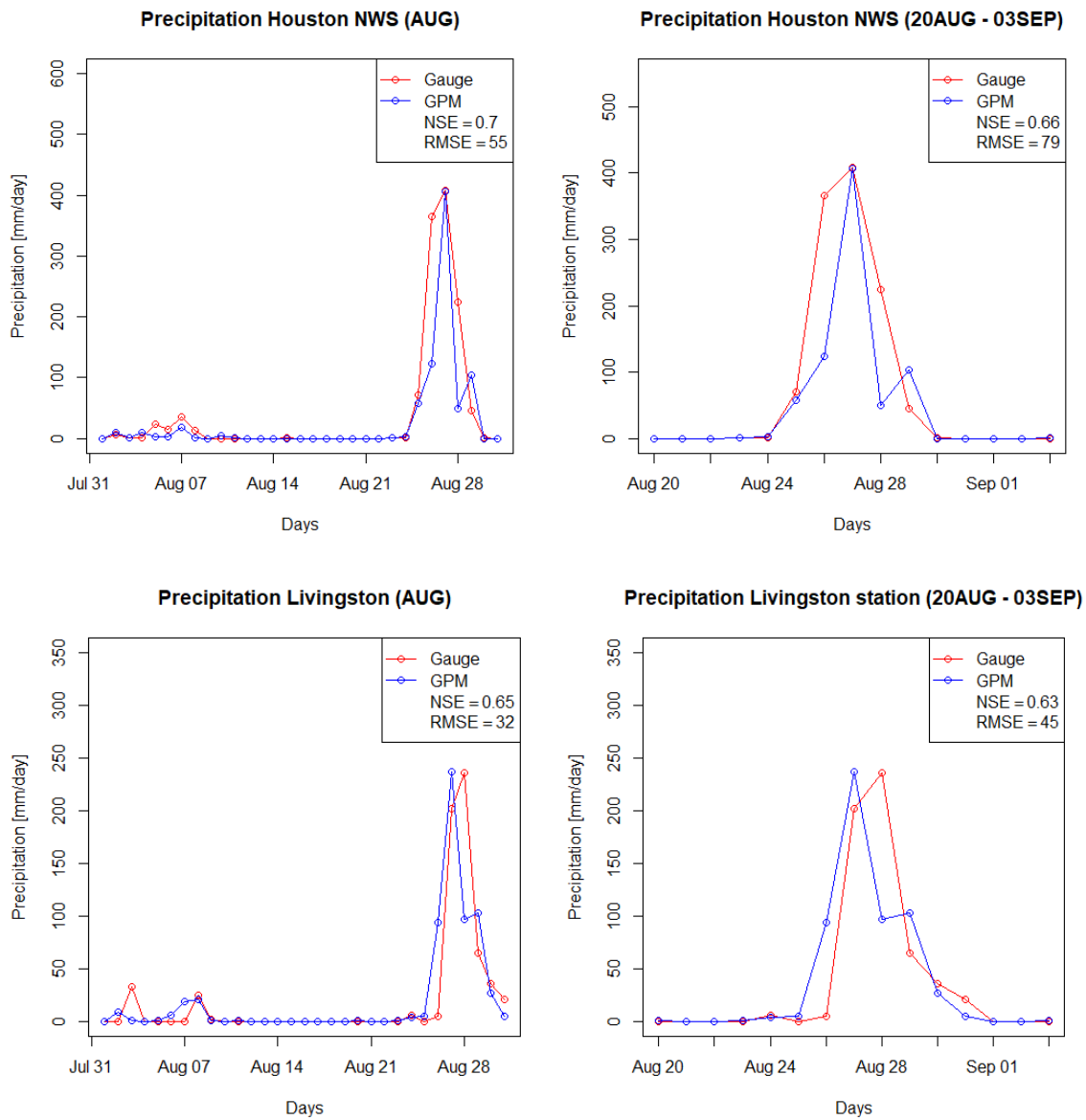


Figure 5.3: Time-series of daily precipitation for GPM and gauges during August and 20 August – 03 September.

Monsoon stations - India

The monsoon stations in India show that the precipitation is hard to measure during large timescales. The precipitation often increases fast to high peaks but drop shortly after (Figures A7-A9). The plots of Dhubri and Jorhat indicate that the GPM often overestimates the precipitation respective to their gauges. However, some peaks are almost correctly captured by the GPM. The timeseries of Shillong show that the GPM is able to capture the precipitation, this is most apparent at the August time scale, where the precipitation peak on 11 August is almost correctly captured, however it is one day too early and there is a minor underestimation of 15 mm (Figure 5.4).

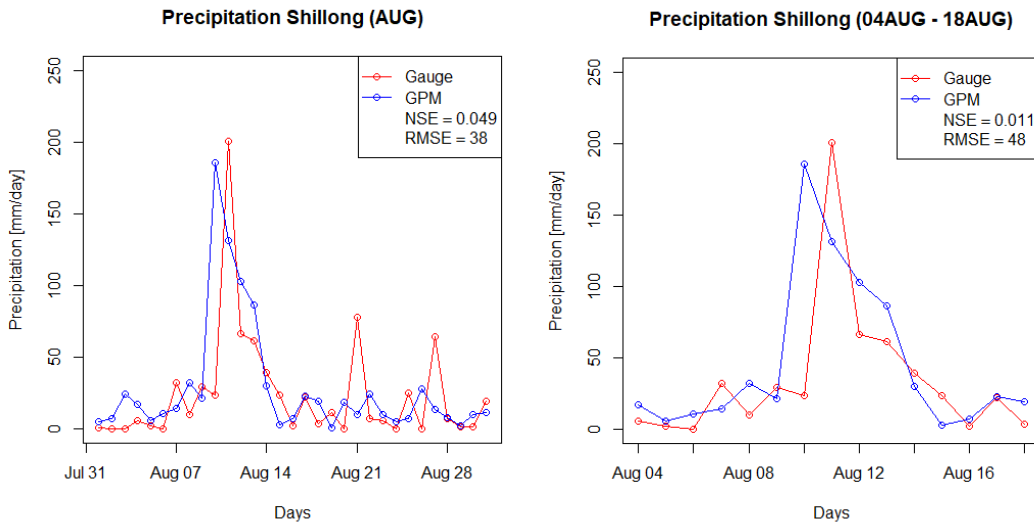


Figure 5.4: Time-series of daily precipitation for GPM and gauges during August and 4 -18 August.

Monsoon stations – Bangladesh & Nepal

The GPM captures the precipitation at the Bangladesh stations quite accurately, especially at the Shah Amanat station (Figure 5.5). The GPM correctly captures the precipitation peaks at Shah Amanat, but GPM underestimates the highest peak by about 70 mm. This is different however for the other precipitation events that occur in August, where GPM usually overestimates the precipitation. The precipitation captured at Osmany by the GPM is not as accurate as at Shah Amanat. There is a lot of overestimation and underestimation occurring. However, the GPM does capture the high peak event on the 11th of August, but with an underestimation of 50 mm (Figure A10)

The GPM doesn't capture the precipitation at Tribhuvan as well as at the stations of India and Bangladesh. This is very apparent on the August timescale (Figure A12). The GPM first overestimates the precipitation during the first few precipitation events in August and then underestimates the precipitation after the 15th of August. It should be noted that the total amount of precipitation is considerably less than at the stations in India and Bangladesh (Figure 5.5).

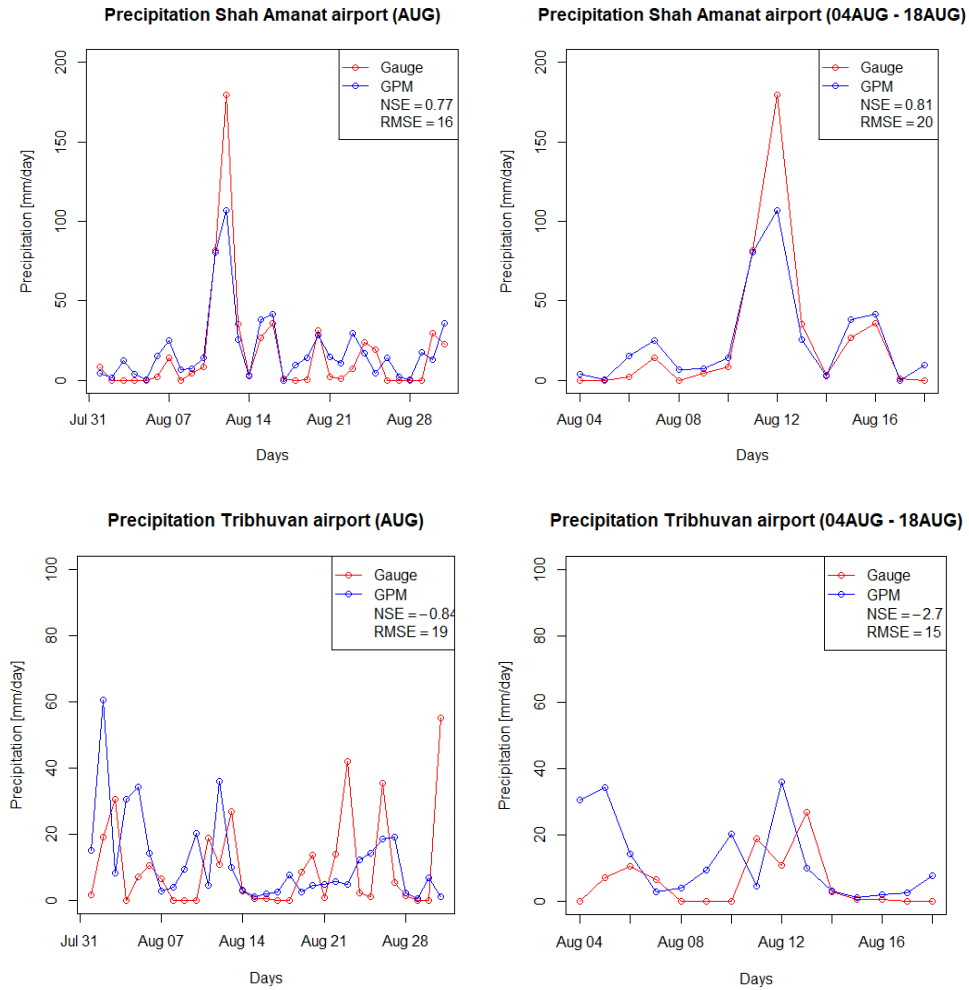


Figure 5.5: Time-series of daily precipitation for GPM and gauges during August and 4 -18 August.

Nash-Sutcliffe efficiency (NSE)

The NSE assesses the predictive power of the GPM respective to the gauges. The NSE values of the USA stations are at the seasonal scale around 0.7 which indicates that the GPM captures the precipitation quite well. However, the NSE coefficient decreases as the timescales get smaller. At the extreme event timescale, the coefficient has decreased to around 0.2 (Table VIII).

The stations in India all have a negative NSE value on the seasonal timescale. The coefficient drops even lower, on the August timescale, for Dhubri and Jorhat. However, it becomes slightly positive for the Shillong station. The coefficient in Dhubri increases to positive values (0.67 and 0.43 respectively) at the two smaller timescales (5 days around extreme event and extreme event). The coefficients in Jorhat and Shillong remain negative and decrease even further during the two smaller timescales.

The NSE values in Nepal all remain positive; however, the values of Osmany are closer to zero, indicating the mean of the GPM is similar to the gauge mean. The values of Shah Amanat are all above 0.5 indicating that the GPM could accurately capture the precipitation (Table VIII).

Root means square error (RMSE)

The RMSE expresses the difference between values of the GPM measurements and observed gauge measurements. The RMSE almost always increases as the timescales get smaller, which is to be expected as the timescales get smaller around an extreme event. This increase leads to high RMSE values, especially at the stations in the USA, where the RMSE peaks at 140. The highest RMSE value of the monsoons station is 88 at the Dhubri station. However, this increase does not apply for three stations: Jorhat, Shah Amanat and Tribhuvan, where the RMSE always remains around a value of 25 (Table VIII).

Table VIII: All statistical indices (NSE and RMSE)

IMERG v5	Seasonal			August			5 days around EE			Extreme event		
	Station	Total prep. [mm]	NSE	RMSE	Total prep. [mm]	NSE	RMSE	Total prep. [mm]	NSE	RMSE	Total prep. [mm]	NSE
Houston NWS	1106	0.71	29	793	0.7	55	743	0.66	79	740	0.15	140
Beaumont	1089	0.72	27	772	0.7	52	634	0.66	79	436	0.15	140
Livingston	899	0.63	18	622	0.65	32	596	0.63	45	534	0.39	77
Dhubri	2108	-1.7	33	675	-6.1	58	533	0.67	73	478	0.43	88
Jorhat	2182	-0.14	22	663	-1.8	24	499	-2.7	20	438	-3.9	20
Shillong	2922	-0.48	33	868	0.049	38	687	0.011	48	527	-0.59	82
Osmany	3002	0.24	25	899	0.22	27	497	0.29	27	309	0.42	30
Shah Amanat	2942	0.62	28	597	0.77	16	377	0.81	20	234	0.74	33
Tribhuvan	1187	-1.2	16	362	-0.84	19	181	-2.7	15	80	-1.9	18

5.2 Comparison hurricane and monsoon

5.2.1 Magnitude & total precipitation

Magnitude & total precipitation – Seasonal and August

The seasonal and monthly precipitation between the two extreme events are quite different as seen in Figure 5.7. The figure shows that precipitation in the monsoon domain has a larger magnitude than the Harvey domain. This is especially apparent on the seasonal scale. Almost the whole monsoon domain contains high precipitation values. But in the Harvey domain, all high values are centralized near Houston. The total precipitation that fell during the seasonal timescale is approximately 40% larger in the monsoon domain than in the Harvey domain (Table IX). The August precipitation maps indicate that there was more precipitation in the hurricane domain (Figure 5.7). This reflects with the total precipitation in both domains: The total August precipitation in the monsoon domain is 402 mm and the total precipitation in the Harvey domain is 697 mm, meaning that there was approximately 75% more precipitation in the Harvey domain (Table IX).

Magnitude & total precipitation – Extreme events and daily

There was abundantly more precipitation during Harvey than during the monsoon event. The differences in the average total precipitation of Harvey and the monsoon are 593 mm and 142 mm respectively (Table IX). A clear difference can also be distinguished in the magnitude of each extreme event; the hurricane has a compact circular form whereas the monsoon precipitation is more spread out. Additionally, this area remains quite stable in the hurricane domain for the seasonal, August and EE timescales (Figure 5.7). Clear differences in magnitude are also noticed between the extreme events on a daily scale (Figure 5.8): Harvey was captured with a circular shape that moves from west to east. The monsoon storm has a rectangular shape that migrates from east to west. The precipitation amount is also quite different between the extreme events, as there was more precipitation during Harvey (Table IX). The extreme events do share a common trait: both extreme events reach their peak precipitation amount during the third day.

Table IX: Total precipitation and peak total precipitation of each domain at different timescales measured by GPM.

Timescale	Harvey domain		Monsoon domain	
	Average total accumulation [mm]	Peak precipitation [mm]	Average total accumulation [mm]	Peak precipitation [mm]
Seasonal	986	1185	1399	3613
August	697	852	410	1091
Extreme event	593	768	142	736
Day 1	37	221	12	133
Day 2	135	289	34	277
Day 3	238	407	42	329
Day 4	89	203	35	309
Day 5	95	235	19	166

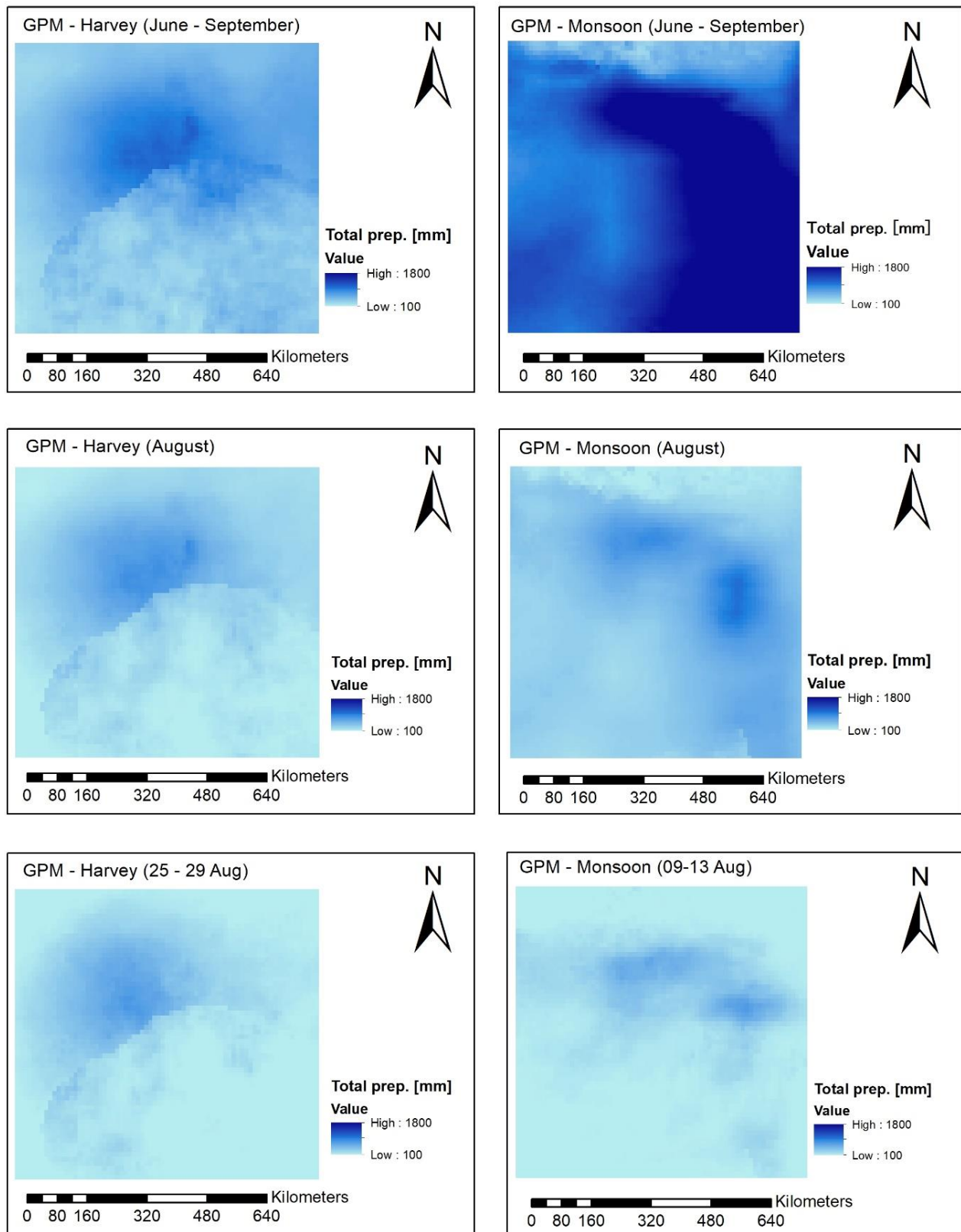


Figure 5.7: Maps of Harvey and Monsoon domain with total precipitation of the seasonal, August and extreme event time scales.
 (Note that the scales are all the same for comparative reasons, meaning that the high values are not indicative for the peaks, actual peaks can be found in Table IX)

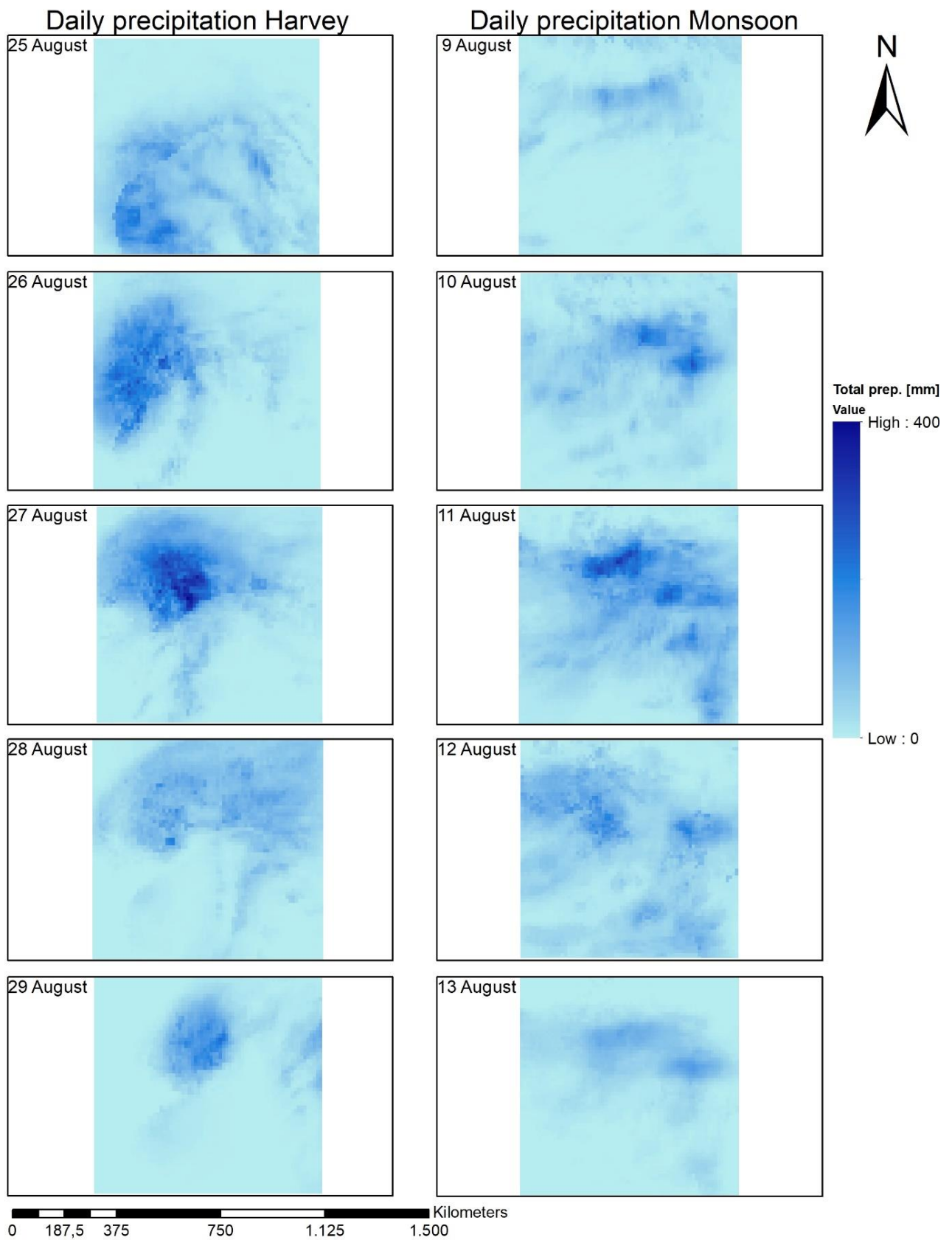


Figure 5.8: Maps of daily precipitation at Harvey and monsoon domain.

Harvey has a larger impact on the total precipitation than the monsoon event. Since Harvey alone caused 60% of the total seasonal precipitation amount, whereas the monsoon event only caused 10% of the total seasonal precipitation amount. This indicates that there were more large precipitation events that occurred in the monsoon domain during June-September and that there was only one large event in the hurricane domain. This is also visible when the seasonal time series plots of Houston NWS and Shillong are evaluated (Figure 5.9). These locations are both located in the center of each extreme event. The precipitation in Houston is relatively low except for the occurrence of Harvey. The Shillong graph shows that there are multiple events occurring during the seasonal time scale.

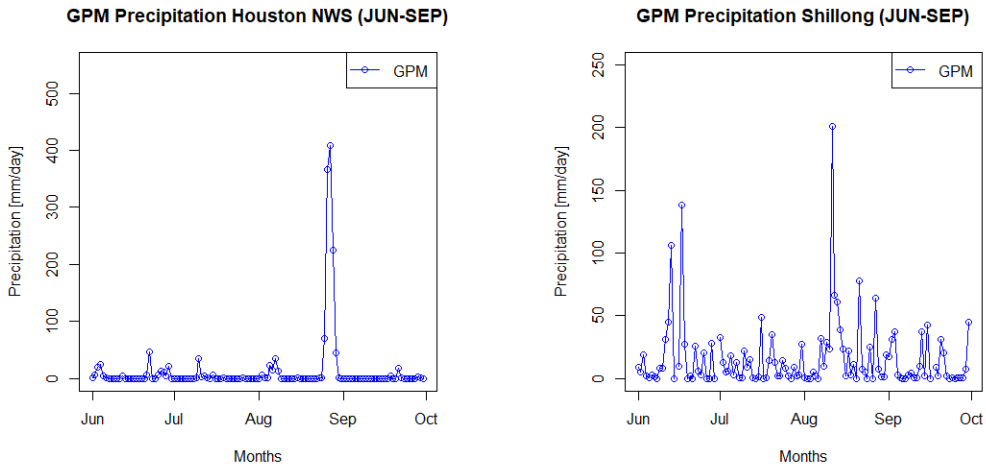


Figure 5.9: Precipitation maps for Houston and Shillong at seasonal scale.

Total precipitation – Double mass plots

The double mass plots indicate that the GPM captures a difference in precipitation accumulation between the extreme events. The monsoon area has a higher total accumulation than the hurricane area (1399 mm and 986 mm respectively). Harvey has a large impact on the total accumulation on the seasonal scale. In figure 5.9 the occurrence of Harvey, as indicated by the red dots, causes large increase in the accumulation of approximately 500 mm. The monsoon event, also indicated by red dots, does not cause this large increase at the monsoon graph. This increase does become visible when the data is evaluated on a monthly scale (Figure 5.9). The monsoon event causes an accumulation increase of approximately 100 mm in a span of five days. It should also be noted that the GPM almost always underestimates the precipitation, however this underestimation fades when the extreme events occur, GPM even overestimates the monsoon event on the monthly scale (Figure 5.9).

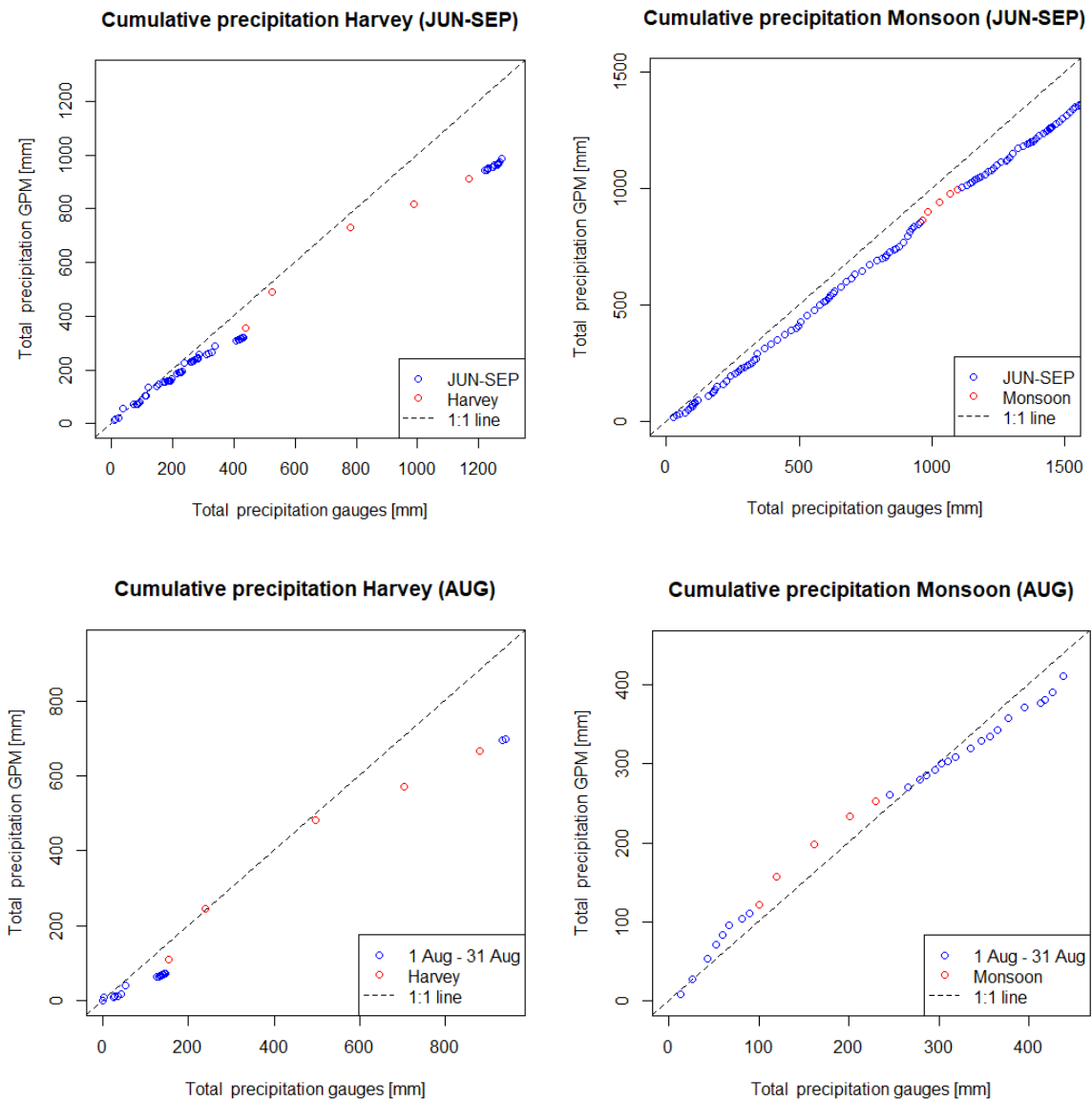


Figure 5.9: Double mass plots of the monsoon event and Harvey for different timescales.

5.2.1 Precipitation rate

Precipitation rate – Seasonal, August and Extreme events

The average precipitation rates during the seasonal timescale indicate that the monsoon domain was a lot wetter than at the hurricane domain (Table X). This can also be observed when the precipitation rates are plotted in each respective grid cell (Figure 5.10). The figure depicts that the higher precipitation rates have a larger spread in the monsoon domain. This is also visible during the August timescale, where the precipitation rates in the monsoon domain are also higher than at the hurricane domain. The monthly peak rates of both domains are around Houston, the Meghalaya and Bangladesh. The extreme events precipitation rates are higher during Harvey than during the monsoon event (Table X). There are also more cells containing high rates in the Harvey domain (Figure 5.10). Indicating that the Harvey's precipitation intensity is higher during the extreme events.

Precipitation rate – Daily

The daily timescales give a better perception of the migration and daily intensity of the extreme events (Appendix A13 & A14). The average precipitation rates of both extreme events are quite similar. However, the peak precipitation rates are higher in the Harvey domain (Table X). The highest precipitation rates occur during the second and third day. The precipitation spread is also the largest during these days, especially during the second day where there are four cells with precipitation rates over 6 mm/h (Appendix A13). The monsoon domain shows that the average precipitation rate ranges from 0.6 to 2.4 and that the peak rates migrate from east to west. The highest precipitation rate occurs on the third day (Table X).

Table X: Maximum. and average precipitation rate of each domain at different timescales measured by GPM.

Timescale	Harvey		Monsoon	
	Max. prep. rate [mm/h]	Avg. prep. rate [mm/h]	Max. prep. rate [mm/h]	Avg. prep. rate [mm/h]
Seasonal	0.4	0.2	0.9	0.5
August	0.9	0.4	1.0	0.6
Extreme event	4.9	1.5	3.7	1.4
Day 1	4.9	1.7	2.4	0.6
Day 2	7.0	1.5	5.3	1.3
Day 3	10	2.0	7.5	2.4
Day 4	4.0	1.4	4.7	1.8
Day 5	5.6	0.7	1.5	0.7

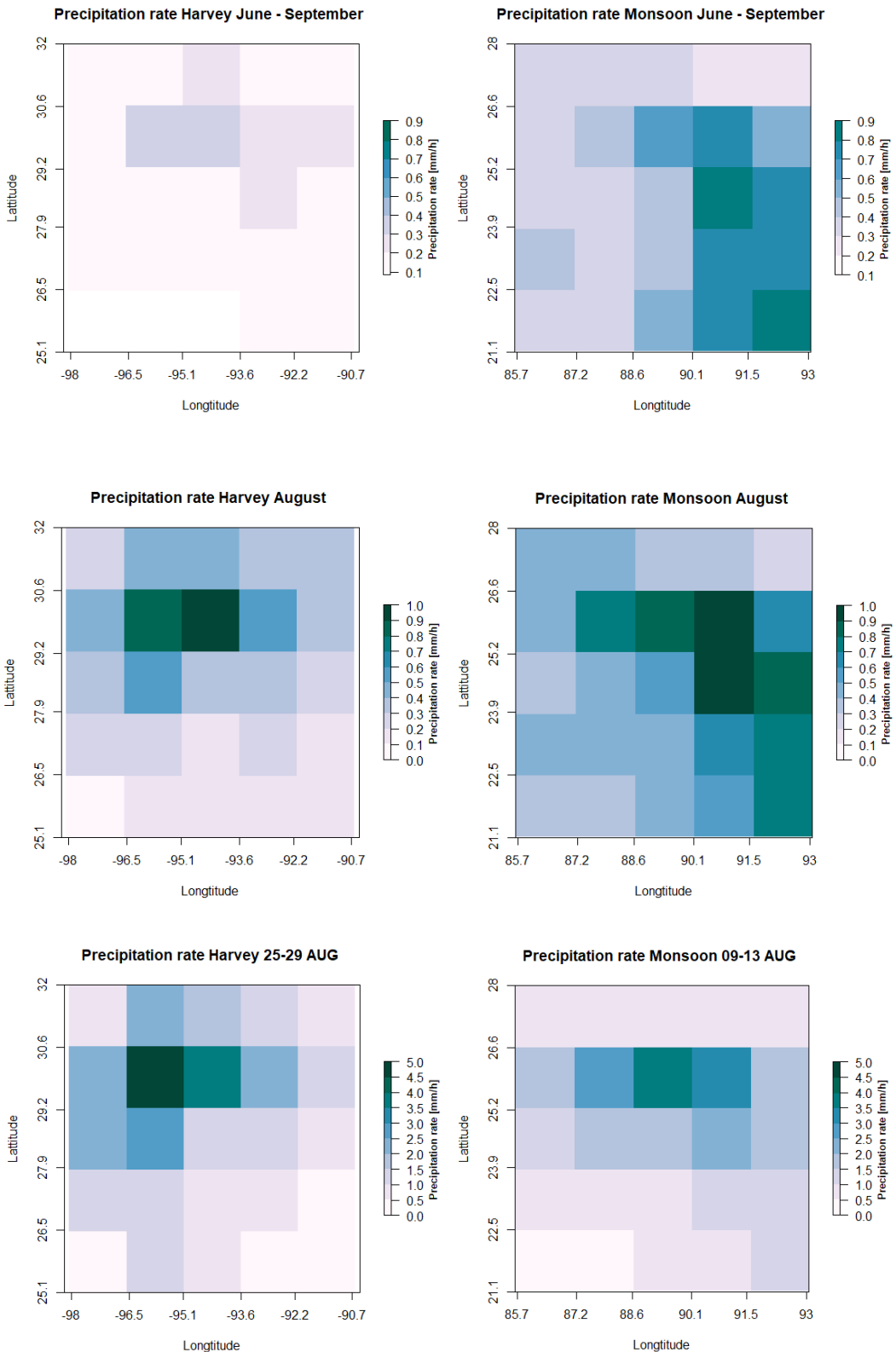


Figure 5.10: Precipitation rate in the Harvey and monsoon domain divided into 25 cells during the seasonal, August and extreme event timescale.

Precipitation rate – Histograms

Histograms of sub-daily precipitation rates were made for both the extreme events. This was done for the month August and of each extreme event. The monsoon precipitation distribution during August is normally distributed, with most precipitation rates of between zero and one mm/h. During the extreme event the distribution changes: the distribution tends to be more evenly distributed as the frequency of higher precipitation rates increases, with more precipitation rates between 1.5 mm/h and 3 mm/h (Figure 5.11).

The frequency distribution of the August histogram for the hurricane area is different than the August monsoon histogram. The frequency of the lowest precipitation rate is a lot higher compared to the higher precipitation rates. This indicates that August was relatively dry period. The extreme event histogram for Harvey indicates that a lot of precipitation occurred during Harvey. The frequency of precipitation rates between 1 mm/h and 3 mm/h are a lot higher than the other precipitation rates. This indicates that Harvey is slightly skewed towards more intense precipitation rates, but not very different from the monsoon event (Figure 5.11).

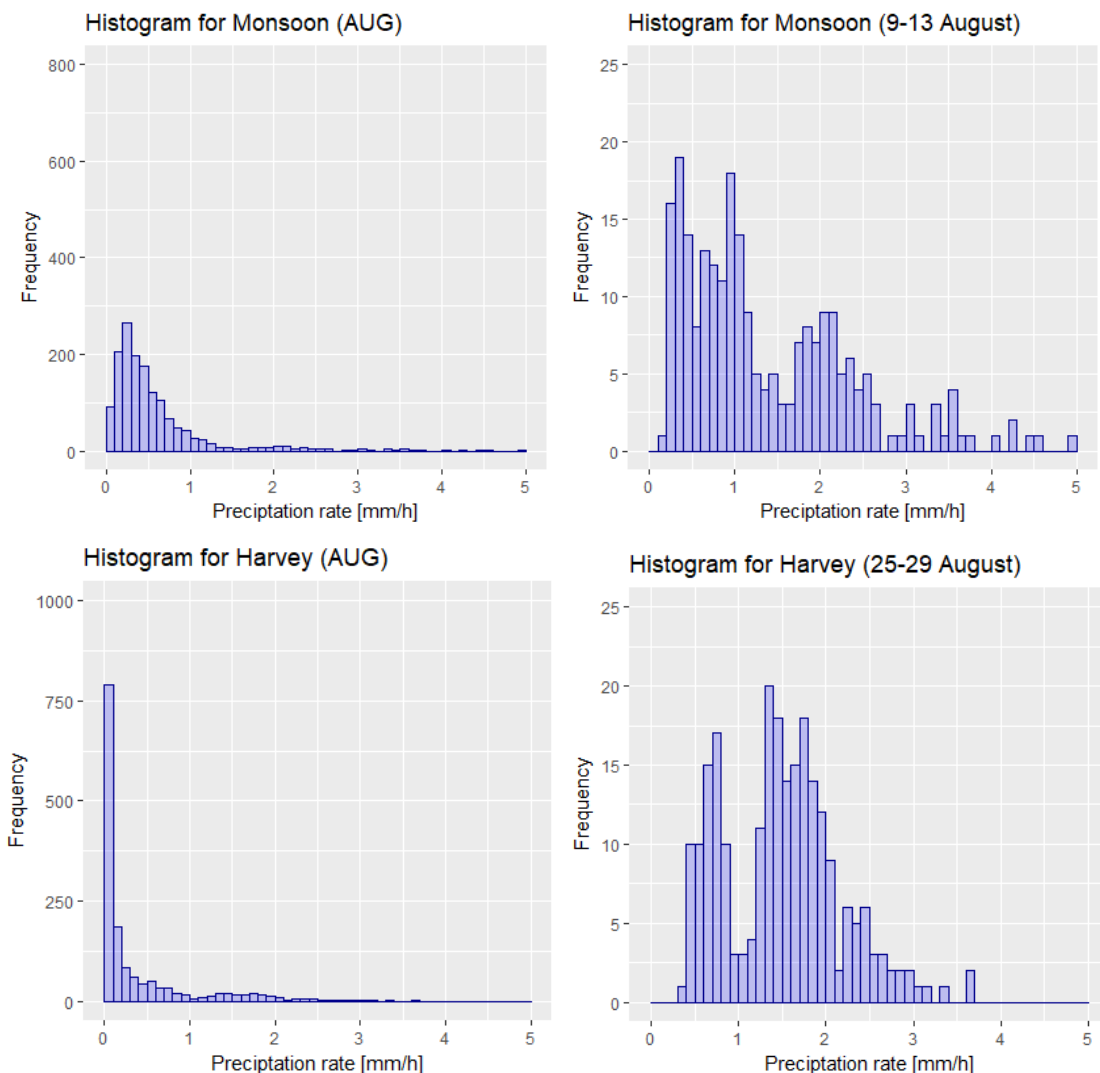


Figure 5.11: Histograms of precipitation rate during August and the extreme event.

5.2.3 Summary: comparison hurricane and monsoon.

The GPM can accurately capture the characteristic differences of the two extreme events.

The magnitudes of Harvey and the monsoon event were quite different. The precipitation magnitude in the monsoon domain is much larger on the seasonal and monthly timescale than in the hurricane domain. The shapes and migration of the extreme events become distinguishable once the precipitation is observed on a daily scale: the hurricane has a circular shape that migrates from west to east and the precipitation is compactly distributed in that shape. The monsoon has a more rectangular shape that migrates from east to west, where the precipitation is quite spread out.

The amount of precipitation that fell during both extreme events is quite different, Harvey had about four times more precipitation compared to the monsoon event. The precipitation that fell during Harvey also had a larger impact (60%) on the total precipitation that fell during June – September, the impact of the monsoon on the seasonal precipitation is 10%. This indicates that there was only one large event in the hurricane domain and that there were more large precipitation events in the monsoon domain during June-September. The double mass plots also indicate this: the jumps in accumulation are larger during Harvey than during the monsoon event.

The average precipitation rates on the seasonal and monthly timescales are a little bit higher in the monsoon domain than in the hurricane domain. This means that the monsoon domain was wetter than the hurricane domain. However, the average precipitation rates during the extreme events are quite similar meaning that the precipitation intensity during Harvey and the monsoon event was similar. The precipitation distribution frequency plots also show these two occurrences.

5.3 GPM accuracy with changing surroundings during extreme event

5.3.1 Monsoon interaction with elevation

GPM and DEM - Monsoon event (9-13 August)

The precipitation measured by the GPM interacts with elevation changes. The precipitation has an increasing trend towards the Himalayas and reaches its maximum at the mountain front of the Himalaya. Most of the precipitation at the green profile falls 350 km inward at an elevation of approximately 850 meters. This is also where the Lesser (lower) Himalaya starts. The precipitation slightly increases again at 450 km where the Greater (higher) Himalaya starts, which is approximately at an elevation of a 1000 meters. The precipitation decreases afterwards further on the higher slopes of the Greater Himalaya. The red profile depicts that the precipitation falls before the Himalaya mountain range; it should be noted that this profile doesn't have the initial elevation increase due to the Lesser Himalayas. Most of the precipitation (>200 mm) occurs right on the mountain front of the Greater Himalaya 330 km inward at an elevation of approximately 250 meters. The peak precipitation is about 100 km from first significant topography. It should also be noted that the precipitation amount of the red profile is larger than at the green profile (Figure 5.11). The situation of the blue profile is different. The peak precipitation occurs earlier at the Meghalaya, which has an elevation of 1490 meter. The precipitation trend of the blue profile is almost parallel to the elevation of the Meghalaya (Figure 5.11). Therefore, it can also be stated that the precipitation of the blue profile can also be linked to elevation.

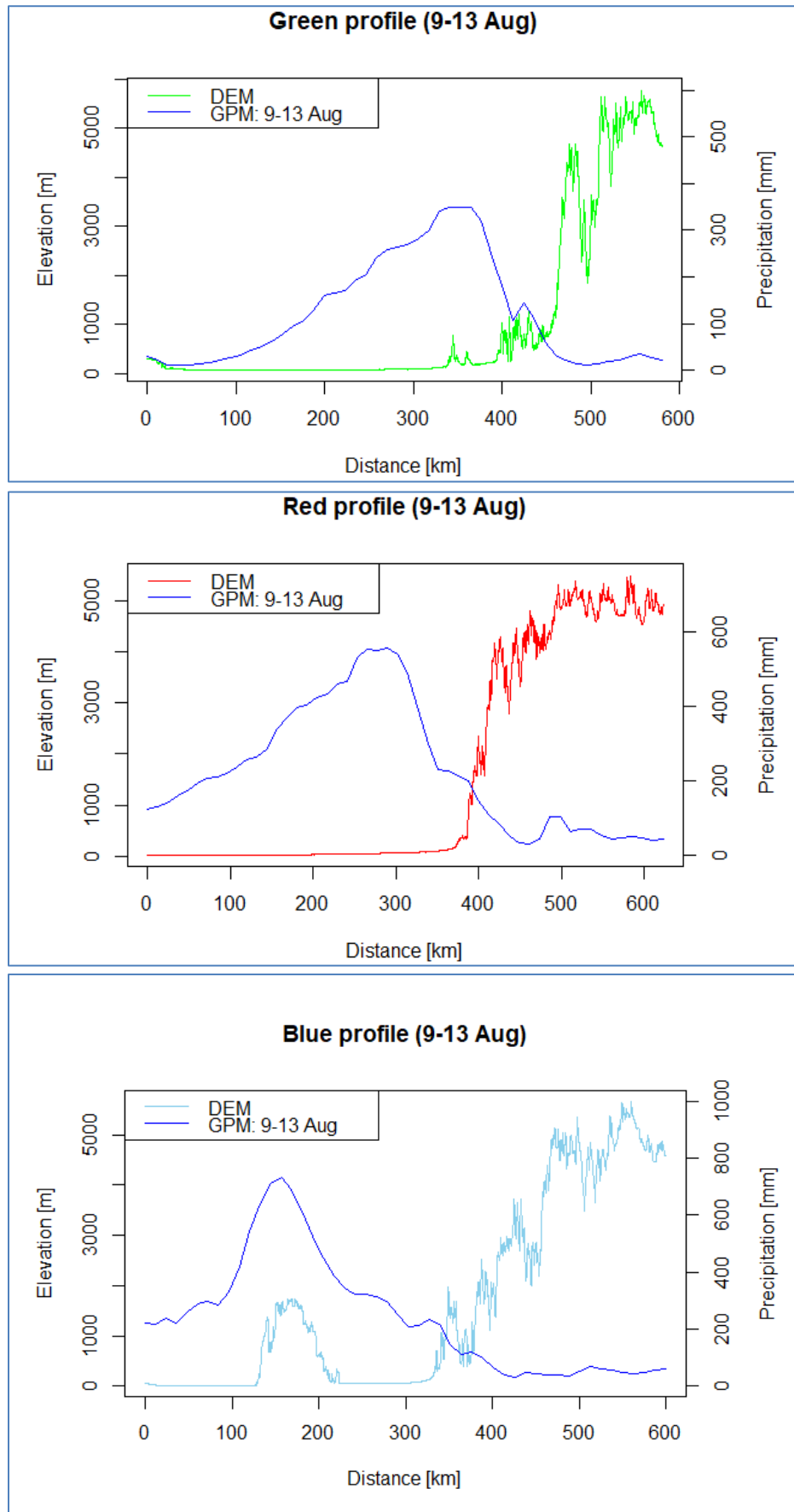


Figure 5.11: DEM and GPM precipitation plotted for the monsoon event (9-13 August)

GPM and DEM – Daily monsoon precipitation plots (9-13 August)

As stated before, GPM captures the monsoon event migrating from east to west on a daily scale. This also can be observed in the green profiles (Figure 5.12). The precipitation steadily increases until reaching a maximum at the 12th of August and decreases on the last day as the precipitation has migrated west of the green line. During the span of these five days an increasing trend of precipitation towards the slope of the Himalayas can be observed. The distance between the peak precipitation and the first significant elevation (380 km inward at the lesser Himalaya) decreases as the monsoon event passes over the green profile. During the first day the peak precipitation occurs after this point, however the precipitation does fall on the slope of the lesser Himalaya. Please note that the precipitation is quite low since the storm has not reached the profile line yet. The second day has two precipitation peaks: the first one is 150 km from the first significant elevation point and the second peaks is exactly at the start of the Lesser Himalaya. The precipitation peaks are all at the 380-km mark during the last three days (Figure 5.12).

The increasing precipitation trend towards the Himalayas can also be observed at the red profiles (Figure 5.13). However, the decrease in precipitation starts earlier, as the red profile is situated in the center of the monsoon event. Hence, the highest precipitation of the red profile occurs during the third day of the monsoon event. The daily distance between the peak precipitation and the first significant elevation (370 km inward at the slope of the Greater Himalaya) varies during the monsoon event. These distances are approximately 65 km, 102 km, 68 km, 154 km and 218 km for each respective day during the monsoon event (Figure 5.13).

The precipitation at the blue line stays is relatively stable as opposed to the green and red line. All heavy precipitation occurs around the Meghalaya, with precipitation totals reaching 200 mm per day (Figure 5.14)

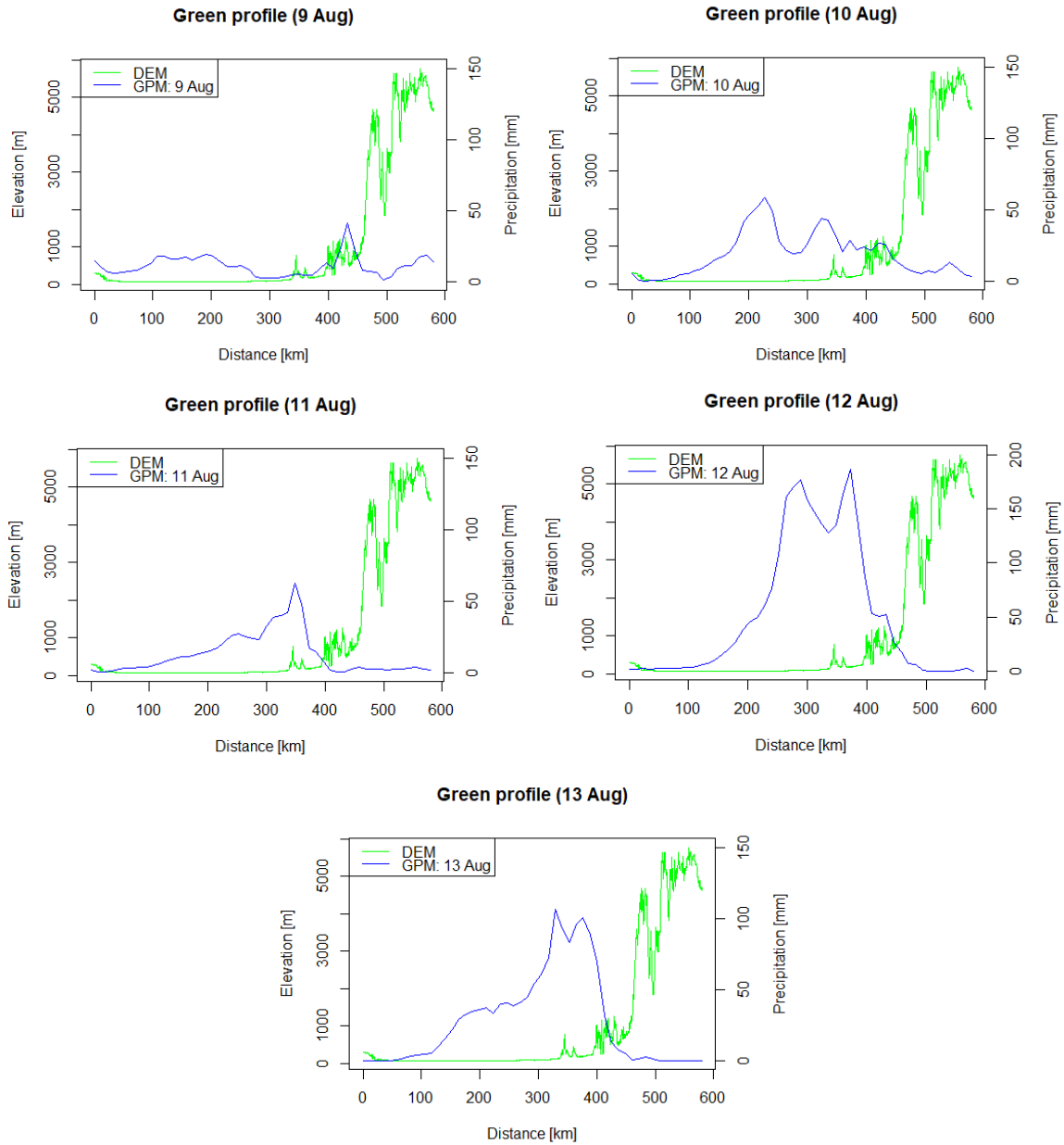


Figure 5.12: DEM and daily GPM profile plots for the green profile at the monsoon area.

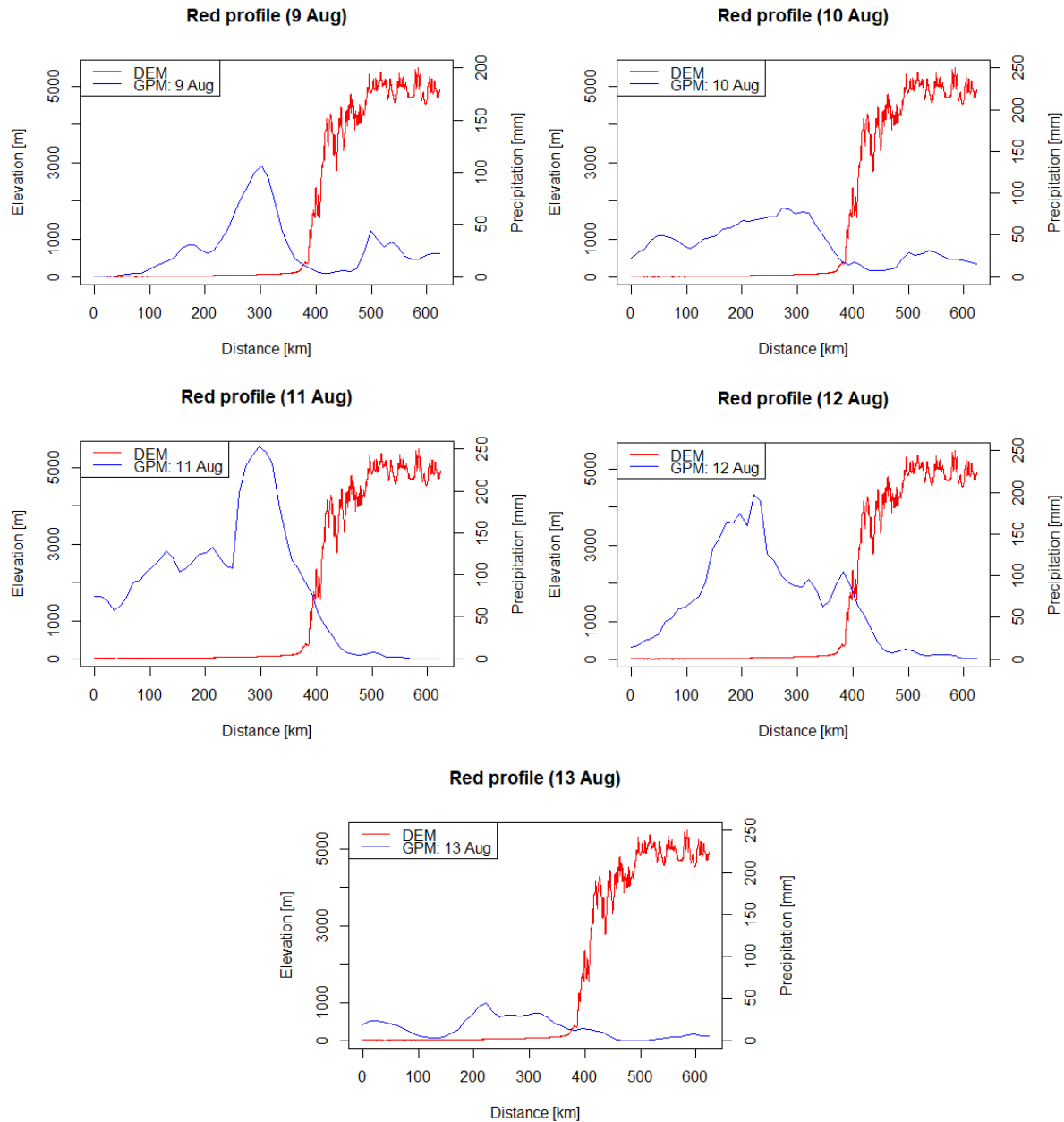


Figure 5.13: DEM and daily GPM profile plots for the blue profile at the monsoon area.

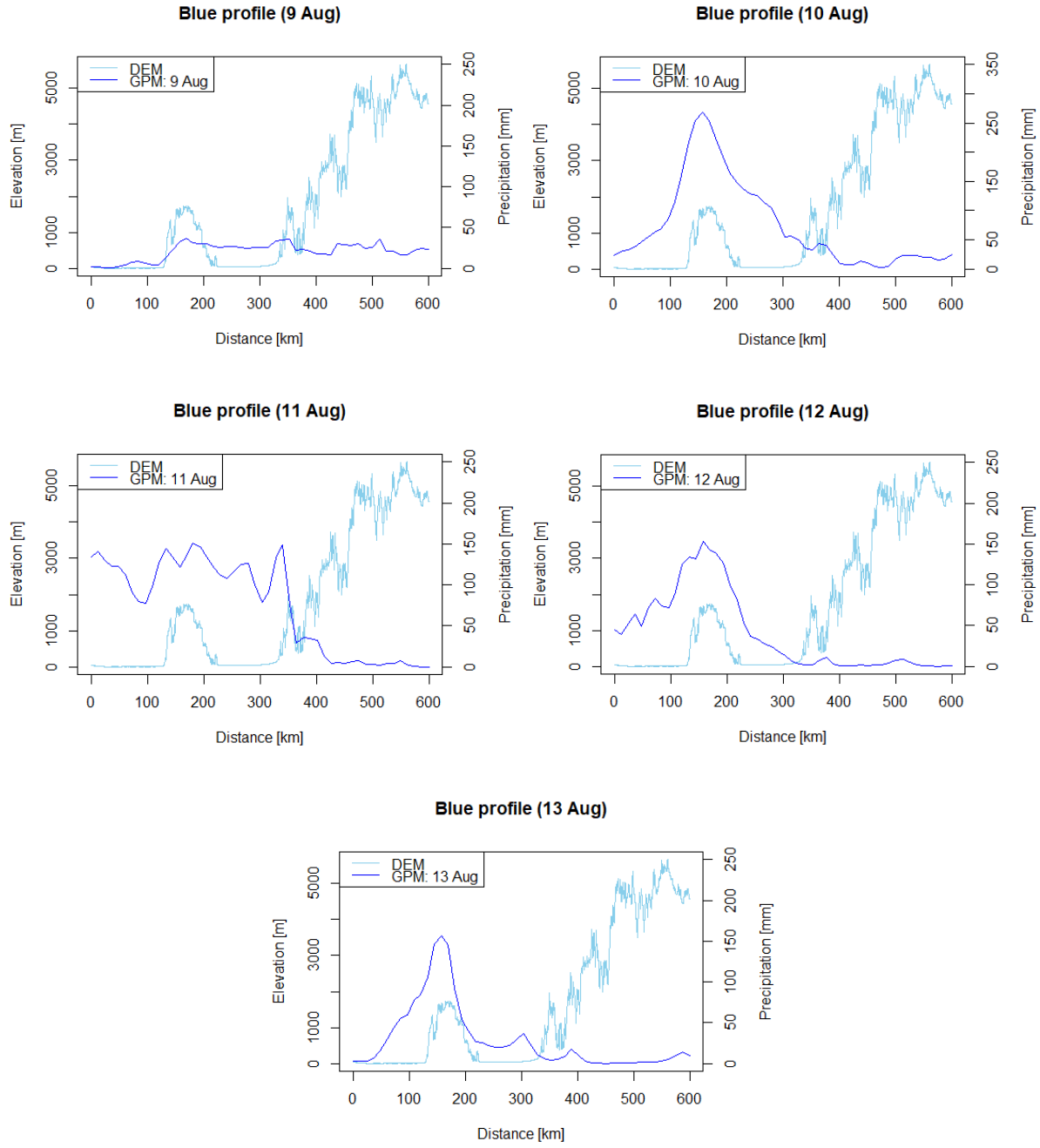
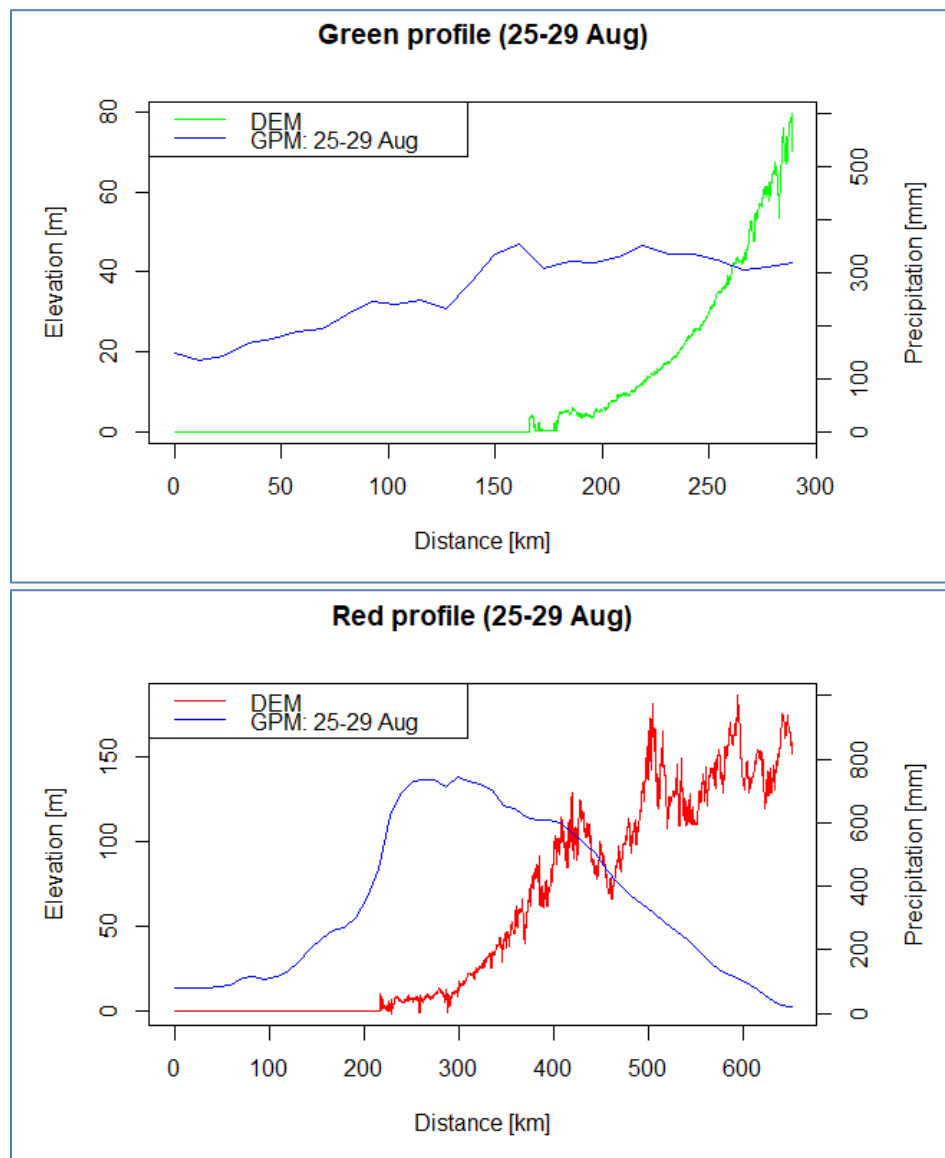


Figure 5.14: DEM and daily GPM profile plots for the blue line at the monsoon area.

5.3.2 Harvey interaction with land

GPM and DEM - Harvey (25-29 August)

As Harvey moved from ocean to land an increase in the amount of precipitation can be observed, indicating hurricane landfall precipitation (Figure 5.15). Most precipitation (353 mm) of the green profile occurred at the 165-km mark which is also where the land-sea transition is located. An increase of approximately 100 mm can be observed here. The red profile shows similar results at the 200-km mark, which is also at the land-sea transition, the precipitation increases with approximately 600 mm to a peak precipitation of 742 mm. The increase is also noticeable at the blue profile where the precipitation increases approximately 600 mm at the 185-km mark to a peak precipitation of 453mm. It should be noted that the elevation of the profiles is exaggerated. The elevation change only amount to about 150 meters for all profiles (Figure 5.15).



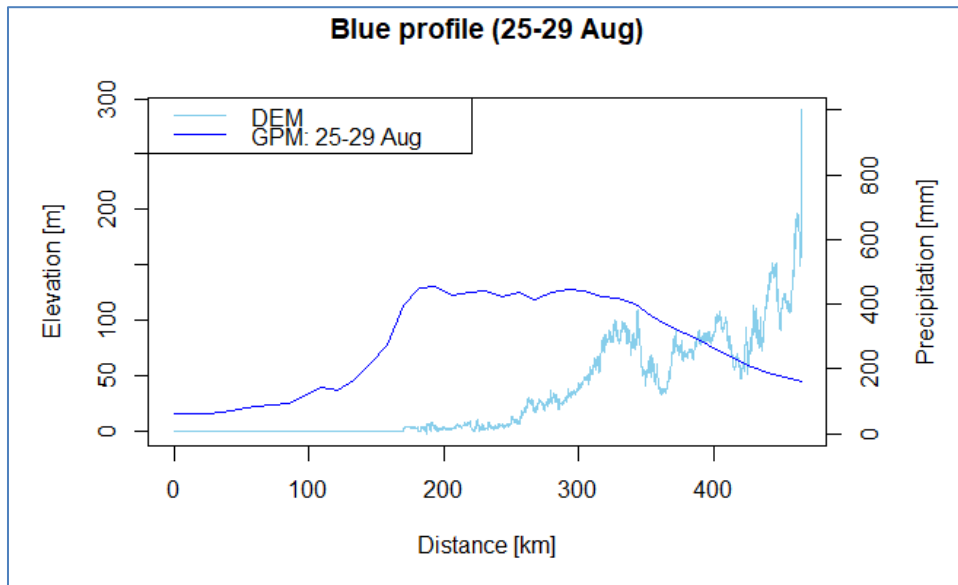


Figure 5.15: DEM and GPM precipitation plotted for Harvey (25-29 August)

GPM and DEM – Daily Harvey precipitation profiles (25-29 August)

The daily precipitation that occurred during Harvey migrates from west to east. This means that only a select few days can represent the hurricane precipitation. For the green profile these are the 25th and 26th of August (Figure 5.16). Harvey is about to make landfall on the 25th, this means that most precipitation is still overseas. On the 26th Harvey has migrated overland towards the green profile. At this point an increase of precipitation can be noticed at the 150-km shore mark. The total precipitation decreases significantly for the last three days as the hurricane migrates eastwards. There is still some precipitation during these days, but most of it falls overseas. The red profile has four days which represent Harvey; these are 26 - 29 August (Figure 5.17). During these four days significant precipitation increase can also be observed at the 200-km land-sea border. These increases are 200 mm, 350 mm, 150 mm and 150 mm for these four days respectively. All days of the blue profile can represent Harvey. During the span of these days an increasing precipitation trend can be observed at the land sea border situated at the 175km mark (Figure 5.18). It should be noted that the precipitation amount is lower than the previous profiles. This is because the blue profile has the most eastwards location and the hurricane has lost most of its power when it reaches this location.

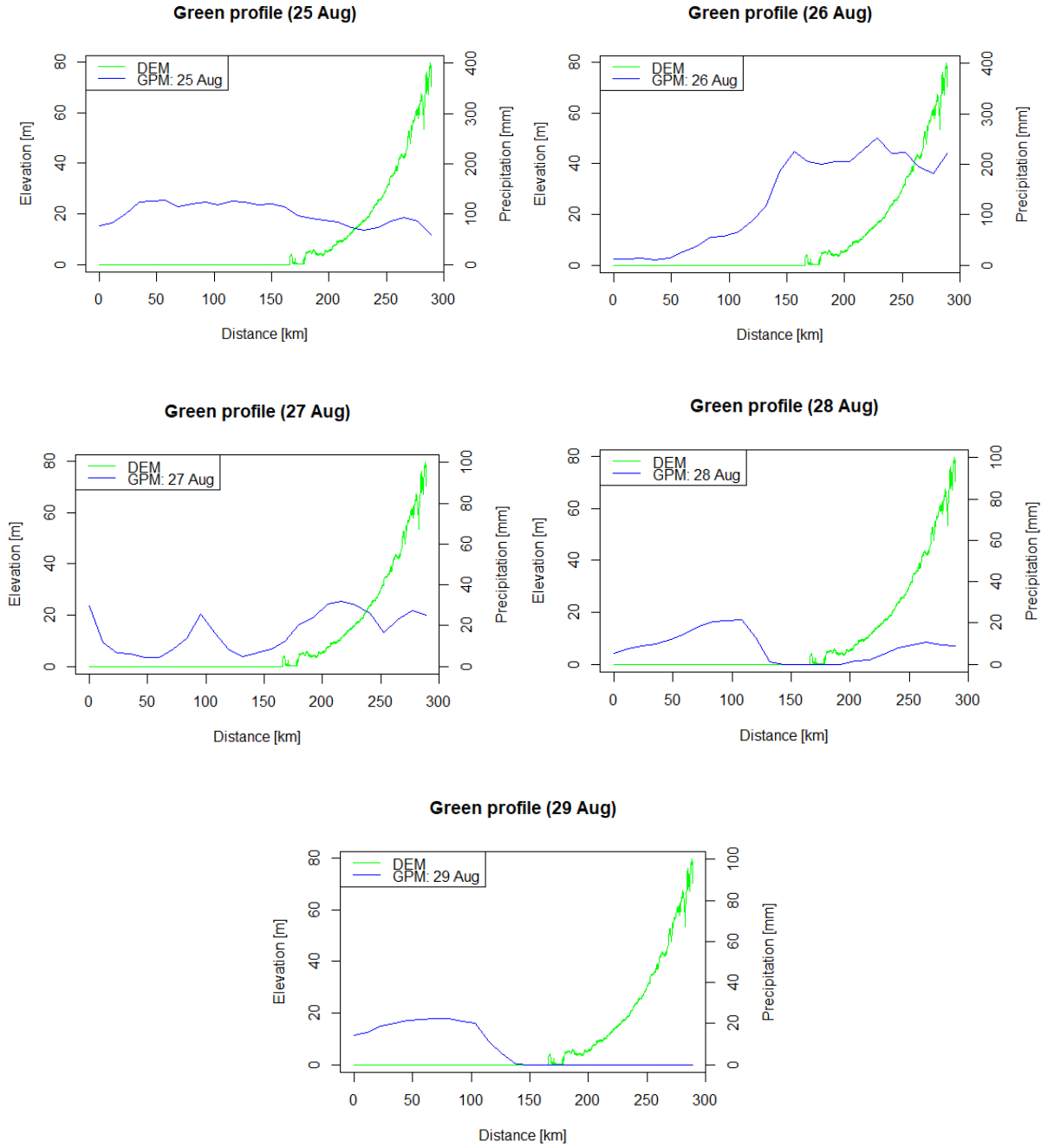


Figure 5.16: DEM and daily GPM profile plots for the green profile at the hurricane area.

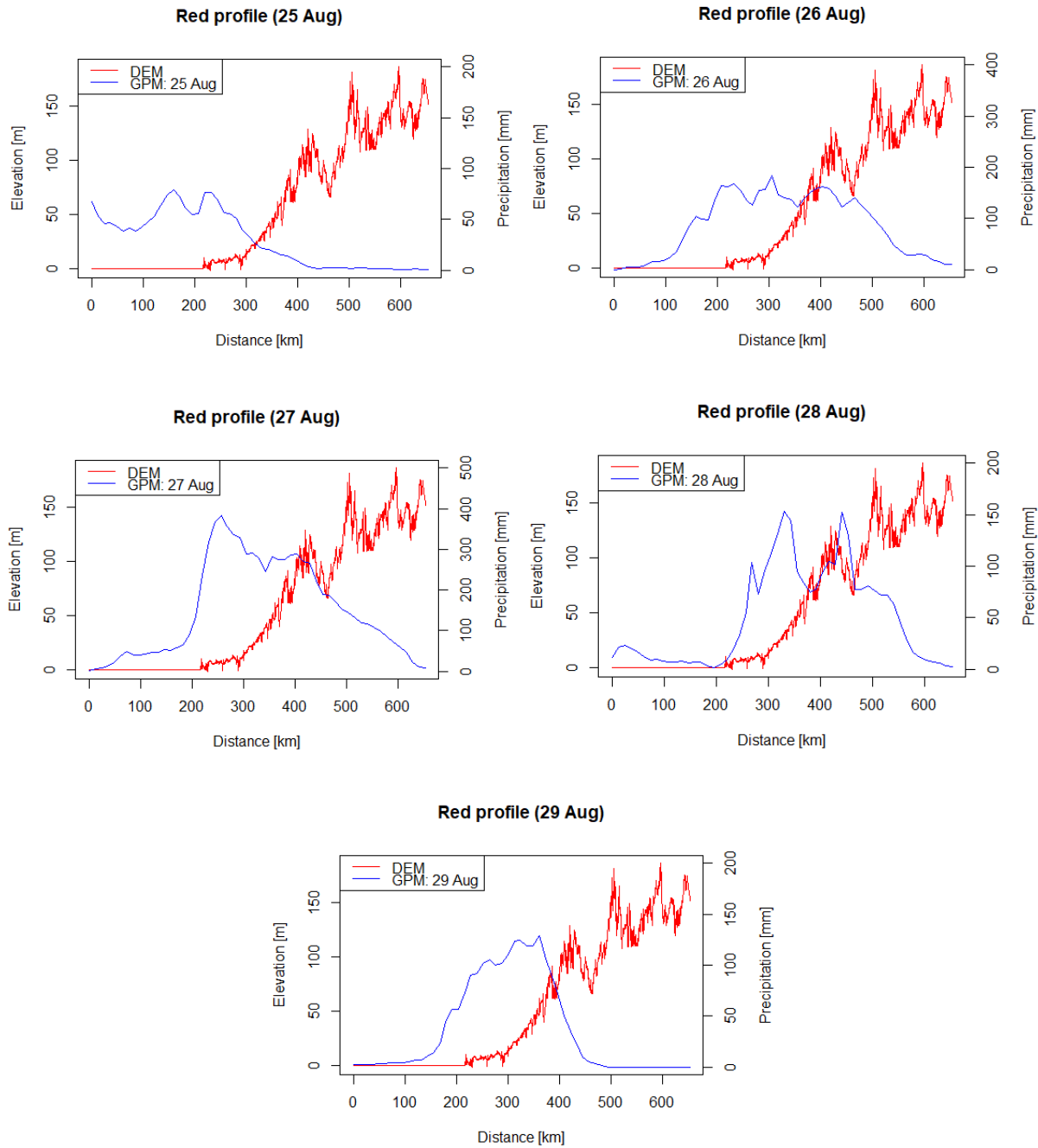


Figure 5.17: DEM and daily GPM profile plots for the red profile at the hurricane area.

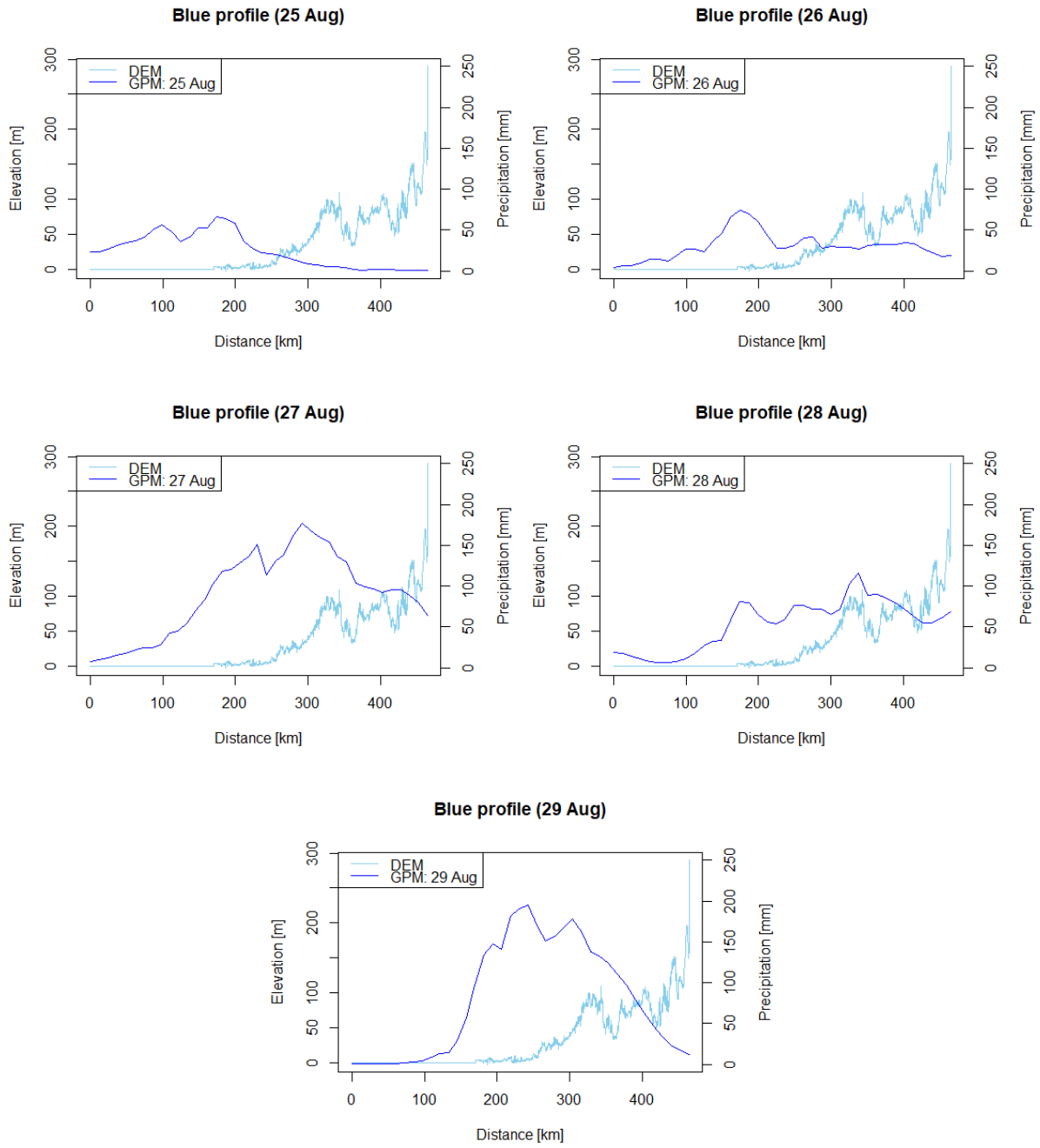


Figure 5.18: DEM and daily GPM profile plots for the blue profile at the hurricane area.

6. Discussion

6.1 Validation

Several studies have been done in the past to test how well GPM captures precipitation against gauges at several locations and under several conditions. A lot of studies state that the GPM is often an improvement over other precipitation measurement methods (Liu, 2016; Ma *et al.*, 2016; Prakash *et al.*, 2016; Sharifi, Steinacker and Saghafian, 2016). However, some papers also show that there GPM still needs some improvements (Liu, 2016; Xu, Shen and Du, 2016; Yuan *et al.*, 2017; Prakash *et al.*, 2018)

Pearson's correlation

The validation of the GPM measurements with the gauges indicates that GPM can accurately capture extreme events. The correlation coefficients calculated during the extreme events show that there is a positive correlation between the two measurement methods: The correlation between the GPM and the gauges during Harvey is 0.78 (Table VI). This concurs with other satellite products such as the TRMM, which had a 0.81 correlation with radar measurements during convective storms (Liao and Meneghini, 2009). The correlation coefficient calculated for the monsoon event indicates that GPM can capture the precipitation, but not as accurate as during Harvey. However faulty gauge values can explain these differences, because the gauge data in the monsoon area can be quite unreliable (Ma *et al.*, 2016; Yuan *et al.*, 2017; Prakash *et al.*, 2018). The correlation between the GPM and the gauges for the monsoon event is 0.58 and ranges from 0.32 to 0.71 in other the timescales (Table VI). However, the correlation coefficient that is calculated in this study shows that GPM is an improvement or compares to other studies conducted in other data-sparse areas. For example, a GPM and TRMM study conducted in Myanmar found coefficients ranging from 0.23 and 0.36 (Yuan *et al.*, 2017). Another GPM study, also conducted in NE-India, showed that the correlation coefficient ranges from 0.45 to 0.70, which concurs with the results found in this study (Prakash *et al.*, 2018).

Bias

However, the correlation plots and negative bias values indicates that the GPM underestimates the precipitation during Harvey (Table VI). This underestimation can be caused by several reasons. The foremost reason is that the data provided by the rain gauges provided are faulty, because the gauges were unable to be emptied on time during Harvey (Blake and Zelinsky, 2018). Another reason could be that the IMERG is faulty. Harvey is a fast and continuous event. An overflying LEO satellite of the GPM-constellation is limited to its data availability and timeliness. This is because a LEO satellite can only make a snapshot of the event, which results in missing sampling input data for the IMERG computation process (Velden *et al.*, 2006). This is also stated in another hurricane study: underestimation of the precipitation up to 50% can be caused due to the turbulence and aspiration in the high winds (and largest rain rates) at the eyewall (Elsberry, 2002). The main reason that the monsoon event does not have this underestimation is the lack of very high windspeeds, this allows the satellites to capture whole monsoon event. The monsoon bias values indicate that the GPM usually overestimates monsoon precipitation (Table VI). This concurs with TRMM measurements studies conducted in mountainous areas (Mei *et al.*, 2014; Prakash *et al.*, 2018). However, most studies state that satellite measurement of the Indian summer monsoon made by GPM and TRMM underestimates the precipitation (Rahman *et al.*, 2009; Prakash *et al.*, 2014, 2018; Yuan *et al.*, 2017). These conflicting results indicate that GPM measurements in mountainous areas are still rather uncertain.

Categorical validation

The categorical validation calculates POD, FAR CSI and ACC values based on the gauge data and GPM data (Table VII). The POD values indicate that GPM can accurately capture precipitation in both domains, with a slightly better accuracy in the monsoon domain. The POD values that were calculated in the monsoon domain range from 0.93 to a perfect 1 value. This indicates that the GPM can capture the occurrence of precipitation in the monsoon domain very well. This result resonates with other satellite precipitation studies that were conducted in the same area where high POD values ranging from 0.75 to 1 were found (Prakash *et al.*, 2014, 2018). The POD values calculated in the hurricane area range from 0.78 to 0.94. This is an improvement compared to another satellite based study conducted in the same area (Nasrin Nasrollahi, 2013). Nasrollahi measured summer precipitation in Texas for four years and found POD values ranging from 0.4 to 0.6. GPM and TRMM studies that were conducted in other areas also found lower POD values: POD values ranging from 0.13 to 0.32 were found in a GPM and TRMM study carried out in Myanmar (Yuan *et al.*, 2017). Another GPM study conducted in the Australian mid-latitudes also measured POD values around 0.4 to 0.6 (Ebert, Janowiak and Kidd, 2007).

Precipitation over time - Harvey

The precipitation timeseries show that GPM can also accurately track the temporal precipitation fluctuations of extreme events. This is especially true for Harvey where this is reflected with the high NSE-values calculated on the monthly timescale (0.7 and 0.65 at Houston NWS and Livingston, respectively). This concurs with another study that researched temporal changes during extreme precipitation events: A TRMM study conducted in Louisiana looked at the performance of the TRMM during six hurricane events and found that the TRMM was able to track temporal precipitation for these six events (Habib, Henschke and Adler, 2009). It should be noted that the NSE values become worse as the timescales get shorter. However, this can be explained because the NSE is sensitive to extreme values and as the timescales get shorter the extremes become relatively less apparent, thus lowering the NSE values (Legates and McCabe Jr., 2005). It should be noted that some stations still indicate underestimation or has a 1-day prediction error. These errors can be explained also with the reasons mentioned before (faulty gauge data and snapshot measuring of continuous processes).

Precipitation over time - Monsoon

The temporal changes in the monsoon area are not as nicely captured as in the hurricane area. Figures 5.4 and 5.5 show that GPM does capture the occurrence of a high precipitation events, however the peaks are not captured correctly. The peaks are often overestimated or estimated a day too early or late. This is especially true for the timeseries of the India and Nepal stations, only the stations situated in Bangladesh appear to correctly capture temporal changes during the monsoon extreme event. This is also reflected in their NSE-values as they are all negative, except for the Bangladesh stations (Table VIII). This doesn't reflect with other studies where temporarily changes were captured very nicely. Past GPM and TRMM have shown that these satellite products are able to track the temporal precipitation fluctuations of extreme events. For example, Prakash *et al.*, (2018) found that the GPM could correctly track the fluctuations of the daily precipitation in India. Another GPM/TRMM study also showed that the satellites products could estimate the temporal precipitation fluctuations in Myanmar on monthly and daily timescales (Yuan *et al.*, 2017).

The most probable reason for the difference in GPM's capability to capture temporal changes are the gauges that were used for the validation. Some gauges are obtained from the GHCN database and others from the GSOD database. GPM uses GHCN monthly gauge data for re-calibrating its estimates (Huffman *et al.*, 2018). This creates a bias in the validation, since the gauges are not independent. This is especially true for the gauges in Texas and Bangladesh. The timeseries at these locations all consists out of GHCN gauges and the peaks and temporal fluctuations are correctly estimated by the GPM. Furthermore, Bangladesh lacks rain gauges compared to the other countries. It could be stated that the re-calibration of the GPM data in Bangladesh would be relatively stronger because there are less gauges to calibrate, creating a bias. Another reason could be that the rain gauges in Bangladesh and Texas are maintained better than in NE-India and Nepal.

6.2 Characteristics: Monsoon vs Harvey

Magnitude

The GPM is good at capturing the different characteristics between the monsoon and Harvey. The GPM could accurately capture the magnitude of Harvey and the monsoon event. Harvey migrated from west to east and the GPM was able to capture this migration pattern (Blake and Zelinsky, 2018). This is along the lines of other satellite precipitation studies that estimated the hurricane tracks correctly (Habib, Henschke and Adler, 2009; Wu *et al.*, 2016). The GPM captured the monsoon event migrating from east to west. This is in accordance with other monsoon studies, as the main water source of the monsoons is the Bay of Bengal (Gadgil, 2003; Yang *et al.*, 2004; Rahman, Sengupta and Ravichandran, 2009). It is also worth noting that most of the precipitation falls east and decreases as the storm migrates west due to being closer to the precipitation source (Bookhagen and Burbank, 2010).

Total precipitation

The GPM estimates the total precipitation that fell during Harvey at approximately 593 mm with a peak precipitation of 786 mm. This is according to NWS-measurements an underestimation, Harvey is the most significant rainfall hurricane event in US history, the hurricane had precipitation peaks up to 1500mm measured at several weather stations (Blake and Zelinsky, 2018). For context, hurricane Rita made landfall in Louisiana in 2004 but only had a total rainfall accumulation that reached 120-230 mm (Habib, Henschke and Adler, 2009). Monsoon are often looked on a seasonal scale, since there is a lot of variability between each individual storm. The GPM measured that the seasonal precipitation at the monsoon domain is 1399 mm. This is in accordance with a study that researched the precipitation in the same area and found an average seasonal precipitation total ranging from 1000 to 2500 mm (Gadgil, 2003).

Intensity

The GPM precipitation rates measured during Harvey can be categorized as very high, with peak rates of 7-10 mm/h on the 26-27 Aug respectively (Table X). However, these are most likely underestimations of the actual peak rates as larger precipitation rates were documented (Blake and Zelinsky, 2018). The temporal fluctuations of the daily precipitation rates seem very reasonable as the second and third day are also documented as the days where the intensity was largest (Blake and Zelinsky, 2018). The monsoon rates on all timescales range from 0.5 to 2.4 mm/h. This concurs with other studies conducted in the same area: precipitation rates ranging from 0.25 to 4.25 mm/h were measured in Nepal and rates

ranging from 0 to 2 mm/h were found in India (Houze, Wilton and Smull, 2007; Pokharel and Hallett, 2015).

The GPM rates measured in the monsoon domain are higher than the hurricane domain rates on the seasonal scale, which is logical as monsoons are characterized as long periods with many precipitation events (Gadgil, 2003). The monsoon daily precipitation rates are lower than Harvey precipitation rates, but are in the same magnitude. But as stated before, the Harvey precipitation rates are probably underestimated and should be of a larger magnitude: A hurricane is usually described as a mesoscale extreme event with high intensity wind speed and precipitation (Barnes *et al.*, 1983). However, hurricane Harvey was an unprecedented large event that it was described as a minor synoptic scale event (Blake and Zelinsky, 2018).

6.3 GPM accuracy with changing surroundings

Monsoon - orographic precipitation

The monsoon event precipitation mostly falls before the mountain front of the Himalayas. All three profiles show that the precipitation increases at the first significant elevation rise (orographic precipitation). This occurs in the green profile at the Lesser Himalaya (350 km inward at an elevation of 850 meter), in the red profile at the Greater Himalaya (450 km inward at an elevation of 1000 meter) and in the blue profile at the Meghalaya (180 km inward at an 1800-meter elevation). These findings correspond with results from other papers involving GPM. There are two types of precipitation that are captured by the GPM at the Himalaya: One which falls on the Lesser Himalayas and one the Greater Himalaya (Bookhagen and Burbank, 2006, 2010). This concurs perfectly with the results from the green and red profiles. The blue profile also shows that there is a link between elevation and precipitation. This finding concurs with other satellite precipitation studies. For example, a TRMM study researching orographic precipitation stated that the interaction between the Meghalaya topography and the air flows originating from the Bay of Bengal is thought to be a primary cause of heavy precipitation in this region (Sato, 2013). These findings conclude that GPM is accurate in mountainous areas.

Harvey - hurricane landfall precipitation

The GPM captured a clear difference between the precipitation amount overland and overseas during Harvey: the precipitation overland is much larger than overseas during the extreme event. This border represents the eyewall of Harvey. As hurricanes hit land they usually weaken as energy provided by the warm ocean water halts. However, Harvey was unique in the matter that the hurricane lingered around the Houston area instead of migrating landward (NWS, 2017; Blake and Zelinsky, 2018). Because the eye stayed above the Gulf of Mexico, Harvey could still draw energy from the warm ocean water while causing heavy precipitation inland and remaining relatively dry in the above the ocean. The great difference in precipitation amount is because the location of the hurricane eyewall and not caused by a physical process. This concurs with a past TRMM study that did research on hurricane landfall precipitation. The study concluded that the TRMM was also able to detect hurricane landfall precipitation (Elsberry, 2002). This concludes that the GPM is also accurate at measuring hurricane landfall precipitation.

6.4 Limitations

This research has a few limitations which will be discussed in this section: Firstly, faulty and unreliable stations gauges make the GPM validation hard to interpret. This is especially true in the monsoon area,

where the density of gauges is not ideal and where a lot of data is missing. Furthermore, a lot of the gauges are used to re-calibrate the measurements done by the GPM, giving the validation a bias. For future studies it is recommended to use or set up an independent and trustworthy dense precipitation gauge network. Furthermore, GPM should include more reliable databases in the IMERG calibration calculations to increase its accuracy. Secondly, as stated before GPM is not able to perfectly capture a high intensity event such as Harvey. The GPM vastly underestimates the precipitation of the hurricane. It is recommended for future studies to compare the results with other remote sensing products for extra validation purposes. This can solve the underestimation due snapshotting continuous events, which especially occurs during Harvey. Finally, the three profiles drawn for both study areas don't have to be representative; this is because the water-vapor supply depends on the storm tracks, which isn't always perpendicular to the elevation front (Barros *et al.*, 2004).

7. Conclusion

This study shows that GPM is suitable to use for quantifying and understanding different types of extreme events. However, there are some indications that it still needs some improvements.

The validation shows that GPM is good at capturing precipitation during extreme events compared to other past-satellite projects. With correlation coefficients, on all timescales, ranging from 0.35 to 0.76 in the Harvey domain and 0.32 to 0.71 in the monsoon domain. However, negative biases show that GPM underestimates the precipitation during extreme events that are high-intensity. The categorical validation shows that GPM is very good at detecting precipitation. The POD values are quite high with values ranging from 0.78 to 0.94, but the precipitation detection in the monsoon domain is especially good with values ranging from 0.93 to a perfect 1. This makes GPM one of the most proficient precipitation detection satellite. The timeseries of the GPM shows that it can correctly capture the temporal fluctuations during extreme events. The occurrence and precipitation peaks at stations in Texas and Bangladesh are well estimated by the GPM which is reflected by their high NSE values. However, GPM does have trouble estimating precipitation peaks in India and GPM has trouble correctly capturing the temporal fluctuation in Nepal.

GPM shows that it can differentiate the characteristics between Harvey and the monsoon event. Harvey was shown as a precipitation event which had a circular form that migrated eastwards. The monsoon event was captured as a rectangular storm that moved westwards. Furthermore, GPM could correctly capture the difference between the total precipitation of both extreme events. Harvey was captured as a precipitation event that had exceptionally high precipitation that contributed 60% to the seasonal rainfall and the monsoon as a high precipitation event that contributed 10% to the seasonal rainfall, indicating that it was one of many high precipitation events. The GPM was not able to accurately capture the precipitation rates that occurred during Harvey. GPM underestimated that the precipitation rates that are indicative for an exceptional high-intensity storm such as Harvey. However, GPM was to capture precipitation rates that represent the monsoon event. These range from 0.6 to 2.4 mm/h with a peak precipitation rate of 7.5 mm/h.

GPM is also able to correctly detect precipitation in the monsoon area as it is orographically enhanced. GPM measured that precipitation fell before the mountain front on either the Lesser Himalayas or on the greater Himalayas. Furthermore, the GPM shows the precipitation on the Meghalaya is almost parallel to the topography of the Meghalaya. Additionally, GPM can also correctly estimate hurricane landfall precipitation. GPM showed that the precipitation amount inland is higher than overseas during Harvey. This is because the hurricane eyewall lingered around the shoreline causing the difference in precipitation amount.

This study concludes that GPM is a reliable source for assessing extreme events. However, data quality could significantly be improved by using more and reliable rain gauges to improve the calibration of the IMERG data. Furthermore, it might be useful to also include more GEO-stationary satellites as they remain in the same place and can constantly measure high-intensity events such as a hurricane. GPM still has a lot of potential uses: GPM showed that it can correctly capture precipitation in areas where it is difficult to measure precipitation. Furthermore, GPM indicated that it can capture temporal precipitation variations making GPM useful examining other high precipitation events. If the validation of GPM data has been improved it could also be used as an input variable in precipitation modeling studies.

8. Glossary

ACC – Accuracy index
AMW – Active microwave
CC – Correlation coefficient
CHIRPS – Climate Hazards Group InfraRed Precipitation with Station data
CMAP – CPC Merged Analysis of Precipitation
CMORPH – CPC MORPHing
CORRA – Combined Radar– Radiometer
CPC – Climate Prediction Centre
CRU – Climatic Research Unit
CSI – Critical success index
DEM – Digital elevation map
DMSP – Defense Meteorological Satellite Program
DPR – Dual– frequency Precipitation Radar
EE – Extreme event
ENSO – El Niño Southern Oscillation
FAO – Food and Agriculture Organisation
FAR – False alarm ratio
GEE – Google Earth Engine
GEO –Geostationary satellites
GHCN – Global Historical Climatology Network
GMI – GPM Microwave Imager
GOES – Geo– stationary Operational Environmental Satellite
GPCP – Global Precipitation Climatology Project
GPI – GOES precipitation index
GPM – Global Precipitation Measurement Mission
GSOD – Global Surface Summary of the Day
ICESat – The Ice, Cloud, and land Elevation Satellite
IMERG – Integrated Multi– satellitE Retrievals for GPM
IR – Thermal InfraRed
JAXA – Japan Aerospace Exploration Agency
Ka– PR The Ka precipitation radar
KuPR – Ku precipitation radar
MERIT – Multi– Error– Removed Improved– Terrain DEM
MetOP – Meteorological Operational satellite
MSG – Meteosat Second Generation satellites
NAO – Northern Atlantic Oscillation
NASA – National Aeronautics and Space Administration
NOAA – National Oceanic and Atmospheric Administration
NSE – Nash– Sutcliffe efficiency
NSE – Nash– Sutcliffe Efficiency
NWS – National Weather service
PBIAS – Percent bias
PERSIANN – Precipitation Estimation from Remotely Sensed Information using Artificial Neural Networks
PMW – Passive microwave
POD – Probability of detection
RMSE – Root mean squared error
SASM – South– Asian summer monsoon
TMPA – TRMM Multi– Satellite Precipitation Analysis
TRMM – Tropical Rainfall Measuring Mission
VIS – Visual
WMO –World Metrological Organization

9. Acknowledgements

I would like to express my appreciation to Dr. Walter Immerzeel and Dr. Joseph Shea for their guidance during of this research. The critical and constructive comments given by them have been of great value and are very much appreciated. I also like to thank MSc. Philip Kraaijenbrink for helping me twice with Google Earth Engine which proved to be invaluable. Special thanks to Shane Soogea and Chris Kerklaan for peer-reviewing my research. Finally, Ian and Niels I'd too thank you guys for the free coffee, which I could not have done without.

10. References

- Adler, R. F. et al. (2003) 'The Version-2 Global Precipitation Climatology Project (GPCP) Monthly Precipitation Analysis (1979–Present)', *Journal of Hydrometeorology*, 4(6), pp. 1147–1167. doi: 10.1175/1525-7541(2003)004<1147:TVGPCP>2.0.CO;2.
- Al, J. E. T. et al. (2004) 'CMORPH: A Method that Produces Global Precipitation Estimates from Passive Microwave and Infrared Data at High Spatial and Temporal Resolution', *Journal of Hydrometeorology*, 5(3), pp. 487–503. doi: 10.1175/1525-7541(2004)005<0487:CAMTPG>2.0.CO;2.
- Annamalai, H., Hamilton, K. and Sperber, K. R. (2007) 'The South Asian summer monsoon and its relationship with ENSO in the IPCC AR4 simulations', *Journal of Climate*. doi: 10.1175/JCLI4035.1.
- Arkin, P. A. and Meisner, B. N. (1987) 'The Relationship between Large-Scale Convective Rainfall and Cold Cloud over the Western Hemisphere during 1982-84', *Monthly Weather Review*, pp. 51–74. doi: 10.1175/1520-0493(1987)115<0051:TRBLSC>2.0.CO;2.
- Barnes, G. M. et al. (1983) 'Mesoscale and Convective Structure of a Hurricane Rainband', *Journal of the Atmospheric Sciences*, pp. 2125–2137. doi: 10.1175/1520-0469(1983)040<2125:MACSOA>2.0.CO;2.
- Barros, a. P. et al. (2004) 'Probing orographic controls in the Himalayas during the monsoon using satellite imagery', *Natural Hazards and Earth System Science*, 4(1), pp. 29–51. doi: 10.5194/nhess-4-29-2004.
- Bessho, K. et al. (2016) 'An Introduction to Himawari-8/9—Japan's New-Generation Geostationary Meteorological Satellites', *Journal of the Meteorological Society of Japan. Ser. II*, 94(2), pp. 151–183. doi: 10.2151/jmsj.2016-009.
- Blake, E. S. and Zelinsky, D. A. (2018) 'National Hurricane Center Tropical Cyclone Report: Hurricane Harvey', *National Hurricane Center Tropical Cyclone Report*, (January), pp. 1–76.
- Bookhagen, B. and Burbank, D. W. (2006) 'Topography, relief, and TRMM-derived rainfall variations along the Himalaya', *Geophysical Research Letters*, 33(8), pp. 1–5. doi: 10.1029/2006GL026037.
- Bookhagen, B. and Burbank, D. W. (2010) 'Toward a complete Himalayan hydrological budget: Spatiotemporal distribution of snowmelt and rainfall and their impact on river discharge', *Journal of Geophysical Research: Earth Surface*, 115(3), pp. 1–25. doi: 10.1029/2009JF001426.
- Ebert, E. E., Janowiak, J. E. and Kidd, C. (2007) 'Comparison of near-real-time precipitation estimates from satellite observations and numerical models', *Bulletin of the American Meteorological Society*, 88(1), pp. 47–64. doi: 10.1175/BAMS-88-1-47.
- Elsberry, R. (2002) 'Predicting Hurricane Landfall Precipitation : Optimistic and Pessimistic Views from the Symposium on Precipitation Extremes', *Bulletin of the American Meteorological Society*, 83(9)(May), pp. 1333–1339.
- Farr, T. et al. (2007) 'The shuttle radar topography mission', *Reviews of Geophysics*, 45(2005), pp. 1–33. doi: 10.1029/2005RG000183.1.INTRODUCTION.
- Ferraro, R. R. et al. (1995) 'The Development of SSM/I Rain-Rate Retrieval Algorithms Using Ground-Based Radar Measurements', *Journal of Atmospheric and Oceanic Technology*, pp. 755–770. doi: 10.1175/1520-0426(1995)012<0755:TDOSSR>2.0.CO;2.
- Fleitmann, D. et al. (2007) 'Holocene ITCZ and Indian monsoon dynamics recorded in stalagmites from

Oman and Yemen (Socotra)', *Quaternary Science Reviews*, 26(1–2), pp. 170–188. doi: 10.1016/j.quascirev.2006.04.012.

Funk, C. et al. (2015) 'The climate hazards infrared precipitation with stations—a new environmental record for monitoring extremes', *Scientific Data*, 2, p. 150066. doi: 10.1038/sdata.2015.66.

Gadgil, S. (2003) 'THE INDIAN MONSOON AND ITS VARIABILITY', *Annual Review of Earth and Planetary Sciences*. doi: 10.1146/annurev.earth.31.100901.141251.

Gesch, D. B. et al. (2014) 'Accuracy assessment of the U.S. Geological Survey National Elevation Dataset, and comparison with other large-area elevation datasets: SRTM and ASTER', *Open-File Report*, p. 18. doi: 10.3133/ofr20141008.

Google Earth Engine (2018) 'Google earth engine'. Available at: <https://code.earthengine.google.com/>.

Gorelick, N. et al. (2016) 'Google Earth Engine: Planetary-scale geospatial analysis for everyone', *Remote Sensing of Environment*. The Authors. doi: 10.1016/j.rse.2017.06.031.

Graham, S. and Riebeek, H. (2006a) 'Hurricanes: The Greatest Storms on Earth', <https://earthobservatory.nasa.gov/Features/Hurricanes/>, 1(October), pp. 1–8. doi: 10.1017/CBO9781107415324.004.

Graham, S. and Riebeek, H. (2006b) 'Hurricanes: The Greatest Storms on Earth', <https://earthobservatory.nasa.gov/Features/Hurricanes/>, 1(October), pp. 1–8. doi: 10.1017/CBO9781107415324.004.

Griffith, C. G. et al. (1978) 'Rain Estimation from Geosynchronous Satellite Imagery—Visible and Infrared Studies', *Monthly Weather Review*, pp. 1153–1171. doi: 10.1175/1520-0493(1978)106<1153:REFGSI>2.0.CO;2.

Gupta, H. V. et al. (2009) 'Decomposition of the mean squared error and NSE performance criteria: Implications for improving hydrological modelling', *Journal of Hydrology*. Elsevier B.V., 377(1–2), pp. 80–91. doi: 10.1016/j.jhydrol.2009.08.003.

Habib, E., Henschke, A. and Adler, R. F. (2009) 'Evaluation of TMPA satellite-based research and real-time rainfall estimates during six tropical-related heavy rainfall events over Louisiana, USA', *Atmospheric Research*, 94(3), pp. 373–388. doi: 10.1016/j.atmosres.2009.06.015.

Harding, D. J. and Carabajal, C. C. (2005) 'ICESat waveform measurements of within-footprint topographic relief and vegetation vertical structure', *Geophysical Research Letters*, 32(21), pp. 1–4. doi: 10.1029/2005GL023471.

Harrison, D. L., Driscoll, S. J. and Kitchen, M. (2000) 'Improving precipitation estimates from weather radar using quality control and correction techniques', *Meteorological Applications*. Universiteitsbibliotheek Utrecht, 7(2), p. S1350482700001468. doi: 10.1017/S1350482700001468.

Hong, Y. et al. (2007) 'Evaluation of PERSIANN-CCS Rainfall Measurement Using the NAME Event Rain Gauge Network', *Journal of Hydrometeorology*, 8(3), pp. 469–482. doi: 10.1175/JHM574.1.

Hou, A. Y. et al. (2014) 'The global precipitation measurement mission', *Bulletin of the American Meteorological Society*, 95(5), pp. 701–722. doi: 10.1175/BAMS-D-13-00164.1.

Houze, R., Wilton, D. and Smull, B. (2007) 'Monsoon convection in the Himalayan region as seen by the TRMM Precipitation Radar', *Quarterly Journal of the Royal ...*, 133(October), pp. 937–948. doi:

10.1002/qj.

Huffman, G. et al. (2018) 'Algorithm Theoretical Basis Document (ATBD) NASA Global Precipitation Measurement (GPM) Integrated Multi-satellite Retrievals for GPM (IMERG)', *Nasa*, (December), p. 29.

Immerzeel, W. W. and Bierkens, M. F. P. (2010) 'Seasonal prediction of monsoon rainfall in three Asian river basins: The importance of snow cover on the Tibetan Plateau', *International Journal of Climatology*. doi: 10.1002/joc.2033.

IPCC (2001a) 'Working Group I: The Scientific Basis', *IPCC: Working Group I: The Scientific Basis*, pp. 6–7. Available at: <http://www.ipcc.ch/ipccreports/tar/wg1/518.htm>.

IPCC (2001b) 'Working Group I: The Scientific Basis', *IPCC: Working Group I: The Scientific Basis*, pp. 6–7.

Joyce, R. J. and Xie, P. (2011) 'Kalman Filter-Based CMORPH', *Journal of Hydrometeorology*, 12(6), pp. 1547–1563. doi: 10.1175/JHM-D-11-022.1.

Katsanos, D., Retalis, A. and Michaelides, S. (2016) 'Validation of a high-resolution precipitation database (CHIRPS) over Cyprus for a 30-year period', *Atmospheric Research*. Elsevier B.V., 169, pp. 459–464. doi: 10.1016/j.atmosres.2015.05.015.

Kidd, C. and Huffman, G. (2011) 'Global precipitation measurement', *METEOROLOGICAL APPLICATIONS*, 353, pp. 131–169. doi: 10.1007/978-3-540-77655-0_6.

Kubota, T. et al. (2006) 'Global precipitation map using satelliteborne microwave radiometers by the GSMAp project: Production and validation', *International Geoscience and Remote Sensing Symposium (IGARSS)*, 45(7), pp. 2584–2587. doi: 10.1109/IGARSS.2006.668.

Legates, D. R. and McCabe Jr., G. J. (2005) 'Evaluating the Use of "Goodness of Fit" Measures in Hydrologic and Hydroclimatic Model Validation', *Water Resources Research*, 35(1), pp. 233–241. doi: 10.1029/1998WR900018.

Liao, L. and Meneghini, R. (2009) 'Validation of TRMM precipitation radar through comparison of its multiyear measurements with ground-based radar', *Journal of Applied Meteorology and Climatology*, 48(4), pp. 804–817. doi: 10.1175/2008JAMC1974.1.

Liao, L. and Meneghini, R. (2011) 'A study on the feasibility of dual-wavelength radar for identification of hydrometeor phases', *Journal of Applied Meteorology and Climatology*, 50(2), pp. 449–456. doi: 10.1175/2010JAMC2499.1.

Liu, J. et al. (2015) 'Evaluation of three satellite precipitation products TRMM 3B42, CMORPH, and PERSIANN over a subtropical watershed in China', *Advances in Meteorology*, 2015. doi: 10.1155/2015/151239.

Liu, Z. (2016) 'Comparison of Integrated Multisatellite Retrievals for GPM (IMERG) and TRMM Multisatellite Precipitation Analysis (TMPA) Monthly Precipitation Products: Initial Results', *Journal of Hydrometeorology*, 17(3), pp. 777–790. doi: 10.1175/JHM-D-15-0068.1.

Ma, Y. et al. (2016) 'Similarity and error intercomparison of the GPM and its predecessor-TRMM multisatellite precipitation analysis using the best available hourly gauge network over the Tibetan Plateau', *Remote Sensing*, 8(7), pp. 1–17. doi: 10.3390/rs8070569.

Mei, Y. et al. (2014) 'Error Analysis of Satellite Precipitation Products in Mountainous Basins', *Journal of Hydrometeorology*, 15(5), pp. 1778–1793. doi: 10.1175/JHM-D-13-0194.1.

Menzel, W. P. and Purdom, J. F. W. (1994) 'Introducing GOES-I: The First of a New Generation of Geostationary Operational Environmental Satellites', *Bulletin of the American Meteorological Society*, pp. 757–781. doi: 10.1175/1520-0477(1994)075<0757:IGITFO>2.0.CO;2.

NASA (2017) 'TRMM - Tropical Rainfall Measurement Mission', pp. 1–2. Available at: <https://pmm.nasa.gov/TRMM>.

NASA (2018) 'The Afternoon Constellation - A-Train', pp. 3–5.

Nasrin Nasrollahi (2013) *Improving Infrared based precipitation retrievals algorithms using multi-spectral satellite imagery*. Springer.

National Weather Service (2014) 'National Hurricane Center', NOAA, *National Hurricane Center*, pp. 1–3. Available at: <http://www.nhc.noaa.gov/>.

New, M. et al. (2001) 'Precipitation measurements and trends in the twentieth century', *International Journal of Climatology*, 21(15), pp. 1889–1922. doi: 10.1002/joc.680.

Nicholson, S. E. et al. (2003) 'Validation of TRMM and Other Rainfall Estimates with a High-Density Gauge Dataset for West Africa. Part II: Validation of TRMM Rainfall Products', *Journal of Applied Meteorology*, 42(10), pp. 1355–1368. doi: 10.1175/1520-0450(2003)042<1355:VOTAOR>2.0.CO;2.

NWS (2017) 'Major Hurricane Harvey - August 25–29, 2017', pp. 22–25. Available at: http://www.weather.gov/crp/hurricane_harvey.

Olson, W. S. et al. (2004) 'The Goddard Profiling Algorithm', *NTRS*.

Parkinson, C. L. (2003) 'Aqua: An earth-observing satellite mission to examine water and other climate variables', *IEEE Transactions on Geoscience and Remote Sensing*, 41(2 PART 1), pp. 173–183. doi: 10.1109/TGRS.2002.808319.

Pokharel, A. K. and Hallett, J. (2015) 'Distribution of rainfall intensity during the summer monsoon season over Kathmandu, Nepal', *Weather*, 70(9), pp. 257–261. doi: doi:10.1002/wea.2544.

Prakash, S. et al. (2014) 'An evaluation of high-resolution multisatellite rainfall products over the Indian monsoon region', *International Journal of Remote Sensing*. Taylor & Francis, 35(9), pp. 3018–3035. doi: 10.1080/01431161.2014.894661.

Prakash, S. et al. (2016) 'From TRMM to GPM: How well can heavy rainfall be detected from space?', *Advances in Water Resources*. Elsevier Ltd, 88(December 2014), pp. 1–7. doi: 10.1016/j.advwatres.2015.11.008.

Prakash, S. et al. (2018) 'A preliminary assessment of GPM-based multi-satellite precipitation estimates over a monsoon dominated region', *Journal of Hydrology*. Elsevier B.V., 556(February 2014), pp. 865–876. doi: 10.1016/j.jhydrol.2016.01.029.

Rahman, S., Sengupta, D. and Ravichandran, M. (2009) 'Variability of Indian summer monsoon rainfall in daily data from gauge and satellite', *Journal of Geophysical Research Atmospheres*, 114(17). doi: 10.1029/2008JD011694.

Sato, T. (2013) 'Mechanism of Orographic Precipitation around the Meghalaya Plateau Associated with Intraseasonal Oscillation and the Diurnal Cycle', *Monthly Weather Review*, 141(7), pp. 2451–2466. doi: 10.1175/MWR-D-12-00321.1.

- Schmetz, J. *et al.* (2002) 'An introduction to Meteosat Second Generation (MSG)', *Bulletin of the American Meteorological Society*, 83(7), pp. 977–992. doi: 10.1175/BAMS-83-7-Schmetz-1.
- Sharifi, E., Steinacker, R. and Saghafian, B. (2016) 'Assessment of GPM-IMERG and other precipitation products against gauge data under different topographic and climatic conditions in Iran: Preliminary results', *Remote Sensing*, 8(2). doi: 10.3390/rs8020135.
- Sorooshian, S. *et al.* (2000) 'Evaluation of PERSIANN system satellite-based estimates of tropical rainfall', *Bulletin of the American Meteorological Society*, 81(9), pp. 2035–2046. doi: 10.1175/1520-0477(2000)081<2035:EOPSS>2.3.CO;2.
- Stephens, G. L. *et al.* (2002) 'The cloudsat mission and the A-Train: A new dimension of space-based observations of clouds and precipitation', *Bulletin of the American Meteorological Society*, 83(12), p. 1771–1790+1742. doi: 10.1175/BAMS-83-12-1771.
- Tadono, T. *et al.* (2016) 'Generation of the 30 M-MESH global digital surface model by alos prism', *International Archives of the Photogrammetry, Remote Sensing and Spatial Information Sciences - ISPRS Archives*, 41(July), pp. 157–162. doi: 10.5194/isprsarchives-XLI-B4-157-2016.
- UN (2017) '16 million children affected by massive flooding in South Asia – UNICEF Secretary-General Spokesperson's Office', (September), pp. 1–2. Available at: <http://www.un.org/apps/news/story.asp?NewsID=57455#.Wbuiz7IjFhE>.
- United States Census Bureau (2018) 'Methodology , Assumptions , and Inputs for the 2017 National Population Projections March 2018', (March).
- Vasiloff, S. V. *et al.* (2007) 'Improving QPE and very short term QPF: An initiative for a community-wide integrated approach', *Bulletin of the American Meteorological Society*, 88(12), pp. 1899–1911. doi: 10.1175/BAMS-88-12-1899.
- Velden, C. *et al.* (2006) 'the Dvorak Tropical Cyclone', (August 2006), pp. 1195–1210. doi: 10.1175/BAMS-87-9-1195.
- Webster, P. J. *et al.* (1998) 'Monsoons: Processes, predictability, and the prospects for prediction', *Journal of Geophysical Research: Oceans*. doi: 10.1029/97JC02719.
- Willmott, C. (1982) 'Some comments on the evaluation of model performance', *Bulletin of the American Meteorological Society*, pp. 1309–1313. doi: 10.1175/1520-0477(1982)063<1309:SCOTEO>2.0.CO;2.
- WMO (2017a) 'Oscar - Satellites'. Available at: <https://www.wmo-sat.info/oscar/satellites>.
- WMO (2017b) 'Oscar - Satellites'. Available at: <https://www.wmo-sat.info/oscar/satellites/>.
- Wu, T. C. *et al.* (2016) 'The GSI capability to assimilate TRMM and GPM hydrometeor retrievals in HWRF', *Quarterly Journal of the Royal Meteorological Society*, 142(700), pp. 2768–2787. doi: 10.1002/qj.2867.
- Xie, P. and Arkin, P. A. (1996) 'Analyses of global monthly precipitation using gauge observations, satellite estimates, and numerical model predictions', *Journal of Climate*.
- Xu, S., Shen, Y. and Du, Z. (2016) 'Tracing the source of the errors in hourly IMERG using a decomposition evaluation scheme', *Atmosphere*, 7(12), pp. 1–12. doi: 10.3390/atmos7120161.
- Yamazaki, D. *et al.* (2017) 'A high-accuracy map of global terrain elevations', *Geophysical Research Letters*, 44(11), pp. 5844–5853. doi: 10.1002/2017GL072874.

Yang, S. et al. (2004) 'Upstream subtropical signals preceding the Asian summer monsoon circulation', *Journal of Climate*. doi: 10.1175/JCLI3192.1.

Yuan, F. et al. (2017) 'Assessment of GPM and TRMM multi-satellite precipitation products in streamflow simulations in a data sparse mountainous watershed in Myanmar', *Remote Sensing*, 9(3). doi: 10.3390/rs9030302.